The Astrophysical Journal, 844:5 (30pp), 2017 July 20 https://doi.org/10.3847/1538-4357/aa7897

Constraining the Physical State of the Hot Gas Halos in NGC 4649 and NGC 5846

Alessandro Paggi[1], Dong-Woo Kim[1], Craig Anderson[1], Doug Burke[1], Raffaele D'Abrusco[1], Giuseppina Fabbiano[1], Antonella Fruscione[1], Tara Gokas[1], Jen Lauer[1], Michael McCollough[1], Doug Morgan[1], Amy Mossman[1], Ewan O'Sullivan[1], Ginevra Trinchieri[2], Saeqa Vrtilek[1], Silvia Pellegrini[3], Aaron J. Romanowsky[4,5], and Jean Brodie[5]
[1] Harvard-Smithsonian Center for Astrophysics, 60 Garden Street, Cambridge, MA 02138, USA; apaggi@cfa.harvard.edu
[2] INAF-Osservatorio Astronomico di Brera, via Brera 28, I-20121 Milano, Italy
[3] Department of Physics and Astronomy, University of Bologna, viale Berti Pichat 6/2, I-40127 Bologna, Italy
[4] Department of Physics & Astronomy, San José State University, San José, CA 95192, USA
[5] University of California Observatories, 1156 High Street, Santa Cruz,CA 95064, USA
Received 2016 October 17; revised 2017 May 4; accepted 2017 June 7; published 2017 July 17

Abstract

We present results of a joint *Chandra*/*XMM-Newton* analysis of the early-type galaxies NGC 4649 and NGC 5846 aimed at investigating differences between mass profiles derived from X-ray data and those from optical data, to probe the state of the hot interstellar medium (ISM) in these galaxies. If the hot ISM is at a given radius in hydrostatic equilibrium (HE), the X-ray data can be used to measure the total enclosed mass of the galaxy. Differences from optically derived mass distributions therefore yield information about departures from HE in the hot halos. The X-ray mass profiles in different angular sectors of NGC 4649 are generally smooth with no significant azimuthal asymmetries within 12 kpc. Extrapolation of these profiles beyond this scale yields results consistent with the optical estimate. However, in the central region ($r < 3$ kpc) the X-ray data underpredict the enclosed mass, when compared with the optical mass profiles. Consistent with previous results, we estimate a nonthermal pressure component accounting for 30% of the gas pressure, likely linked to nuclear activity. In NGC 5846 the X-ray mass profiles show significant azimuthal asymmetries, especially in the NE direction. Comparison with optical mass profiles in this direction suggests significant departures from HE, consistent with bulk gas compression and decompression due to sloshing on ∼15 kpc scales; this effect disappears in the NW direction, where the emission is smooth and extended. In this sector we find consistent X-ray and optical mass profiles, suggesting that the hot halo is not responding to strong nongravitational forces.

Key words: galaxies: ISM – ISM: individual objects (NGC 4649, NGC 5846) – X-rays: ISM

1. Introduction

About 85% of the mass of the universe takes the form of invisible dark matter (DM). DM plays a key role in the formation and evolution of galaxies. Numerical simulations based on the cold dark matter (ΛCDM) model (e.g., Navarro et al. 1997) successfully reproduce observed large-scale structures of galaxies through the hierarchical mergers of DM halos with baryonic matter (galaxies) trapped in their gravitational potential. DM also influences the star formation efficiency (e.g., Auger et al. 2010), the major star formation epoch (e.g., Thomas et al. 2005), the growth of supermassive black holes (e.g., Booth & Schaye 2010), and the fate of hot gas (Ciotti et al. 1991; Kim & Fabbiano 2013).

A key test of the ΛCDM predictions is the radial profile of DM halos in galaxies. X-ray observations of the hot interstellar medium (ISM) can be used to measure the total mass within a given radius if the hot gas is hydrostatic equilibrium (HE), but departures from HE can seriously affect mass measurements (e.g., Fabricant et al. 1984; Buote & Humphrey 2012; see also Trinchieri & Fabbiano 1985; Canizares et al. 1987; Fabbiano & Trinchieri 1987; David et al. 1990, 1991; Kim et al. 1992a, 1992b; Buote & Humphrey 2012). Recently, comparisons with mass profiles derived from optical indicators (GCs/PNs) have uncovered significant discrepancies (e.g., see Figure 8 in Pota et al. 2015 for NGC 1407; Figure 7 in Napolitano et al. 2014 for NGC 5846). The high-resolution observations by *Chandra* revealed an increasing number of structural features in the hot ISM (e.g., jets, cavities, cold fronts), putting the validity of the HE assumption in question (Statler 2012; Buote & Humphrey 2012). In addition, gas bulk motions on large scales could cause a significant deviation from the HE, resulting in an incorrect mass profile if azimuthally averaged quantities are applied (Markevitch & Vikhlinin 2007). On small scales, comparisons between X-ray and optical measurements of total mass profiles have shown strong departures from HE, with additional nonthermal pressure components (e.g., Churazov et al. 2008; Johnson et al. 2009; Humphrey et al. 2013; Paggi et al. 2014) that can be as large as ∼40% of the total pressure (Ciotti & Pellegrini 2004; Pellegrini & Ciotti 2006; de Plaa et al. 2012).

The present investigation places itself within this line of research. We study differences between mass profiles derived from X-ray data in the HE assumption and those from more robust optical indicators, to investigate the physical state of the hot ISM and gather hints on galaxy interactions and nuclear feedback. In the following analysis we assume the mass profile from the optical data as the baseline against which we compare the X-ray results. In this first paper, we focus on two early-type galaxies (ETGs), NGC 4649 and NGC 5846. This paper presents in detail the method that we have developed for this analysis and that will be applied to a larger sample of galaxies in the near future. NGC 4649 represents a good example of a relatively relaxed system with symmetric and smooth X-ray mass profiles in fair agreement with optical measurements in the 3–12 kpc range, with only some disturbances in the inner regions, and evidence for ram pressure stripping in the outer part of the galaxy. NGC 5846, on the other hand, is a system where bulk motion of gas introduces some measurable

Table 1
General Properties of the Sources Discussed in This Work

(1) Source Name	(2) R.A. (hms)	(3) Decl. (dms)	(4) Distance (Mpc)	(5) Spatial Scale (pc arcsec^{-2})	(6) $N_{\rm H}$ (10^{20} cm^{-2})	(7) $5R_e$ (kpc)
NGC 4649	12:43:40.0	+11:33:10	15.7	76	2.04	25.1
NGC 5846	15:06:29.3	+01:36:20	23.1	112	4.29	33.0

Note. (1) Source name. (2, 3) Source coordinates. (4) Distance in Mpc. (5) Spatial scale in pc arcsec^{-2} at the distance reported in column (4). (6) Galactic hydrogen column density in the source direction. (7) Five effective radii R_e as reported by Alabi et al. (2016).

deviations in its mass profile from optical data on both small and large scales. For this analysis we use the entire available set of *Chandra* and *XMM-Newton* data, thus combining large radial extent with high angular resolution. When the hot gas distribution is not azimuthally symmetric, we take into account this asymmetry by analyzing the X-ray data in various pie sectors, instead of relying on azimuthally averaged quantities, to derive the most accurate estimate of the density and temperature profiles of the hot gas. We then compare with recent high-quality total mass profiles from optical data, available thanks to integral field spectroscopy and the use of several mass tracers—stellar dynamics (SD), globular clusters (GCs), and planetary nebulae (PNs)—extending to many effective radii (e.g., Deason et al. 2012; Coccato et al. 2013; Cappellari et al. 2015; Alabi et al. 2016; Foster et al. 2016). We explore the systematic uncertainties on the X-ray mass profiles from different analysis techniques, including background subtraction, gas profile fit smoothing, and free element abundances.

The paper is organized as follows. In Section 2 we briefly present the main properties of the objects selected for our analysis. In Section 3 we present the procedure we adopted for the reduction and analysis for *Chandra* and *XMM-Newton* data. In Section 4 we present and discuss the results of our analysis. Finally, in Section 5 we draw our conclusions.[6] For brevity, in what follows we refer to X-ray mass profiles derived under the HE assumption as HE mass profiles.

2. Sample Selection

We selected two well-studied ETGs—NGC 4649 and NGC 5846—in order to test our analysis method and compare the results in the presence of different ISM situations. The main properties of these two galaxies are listed in Table 1.

1. NGC 4649 (M60) is a nearby (∼16 Mpc) X-ray-bright giant elliptical galaxy located in a group at the eastern edge of the Virgo Cluster that harbors a faint nuclear radio source (Condon et al. 2002). On <3 kpc scales (∼40″), small disturbances in the X-ray-emitting gas (Shurkin et al. 2008; Dunn et al. 2010; Humphrey et al. 2013) are related to the nuclear radio emission. These disturbances are also related to discrepancies between the mass profile presented by Shen & Gebhardt (2010)—evaluated from optical (SD and GC) data—and the mass profile obtained from X-ray data. Paggi et al. (2014), making use of the deepest *Chandra* data available, showed that the radio source contributes a nonthermal pressure component accounting for ∼30% of the observed gas pressure.

A recent analysis of *Chandra* data by Woods et al. (2017) showed evidence for ram pressure stripping of the gas in NGC 4649 on scales ≳12 kpc (≳160″), as a consequence of its motion through the Virgo intracluster medium (ICM). In particular, these authors show an edge in the surface brightness profile in the NW direction, consistent with a cold front, and two bent, wing-like structures in the NE and SW directions interpreted as Kelvin–Helmholtz instabilities caused by the motion of the galaxy through the Virgo ICM. In addition, significant anisotropies in the projected 2D spatial distributions of GCs and low-mass X-ray binaries in the outskirts of NGC 4649 have been reported by D'Abrusco et al. (2014), Mineo et al. (2014), and Pota et al. (2015), suggesting that this galaxy has experienced mergers and/or multiple accretions of less massive satellite galaxies during its evolution. Recently, lower limits on the turbulence velocities in the ISM of NGC 4649 have been set by Ogorzalek et al. (2017), making use of deep *XMM-Newton* RGS observations.

Figure 1 shows merged, exposure-corrected, broad-band (0.3–10 keV) images of NGC 4649 data from *XMM-Newton* MOS (left panel) and *Chandra* ACIS (right panel). The left panel shows the *XMM-Newton* merged data with detected point sources indicated with white circles. The right panel of the same figure shows the central region of the source as imaged by *Chandra*. In both panels, the regions used for spectral extraction are indicated in green. Figure 2 shows the same data in the 0.3–2 keV band with different color scales to highlight small-scale (top panel) and large-scale (bottom panel) structures.

The surface brightness profiles within 12 kpc, that is, away from the disturbances reported by Woods et al. (2017), are smooth in all sectors, indicating that on such scales NGC 4649 features a fairly relaxed ISM distribution, with a smooth and symmetric morphology, and only some disturbances in the inner regions of the galaxy. As an example, Figure 3 shows a comparison between the surface brightness profiles in the full (0–360), SW (90–180), and SE (180–270) sectors. In the following analysis we will therefore restrict our analysis to the inner <12 kpc region in order to avoid the regions disturbed by NGC 4649 motion in the Virgo ICM. The complete set of figures is presented in Appendix C.

2. NGC 5846 is the central and brightest galaxy in a group (Mahdavi et al. 2005) located at a distance of ∼23 Mpc (Tonry et al. 2001). It is nearly spherical (E0–1) in shape and is kinematically classified as a slow rotator (Emsellem et al. 2011). NGC 5846 exhibits pronounced disturbances in its ISM morphology, hence posing a serious question as to whether it can be in HE. *Chandra*

[6] In the following all angles are measured from the N direction going counterclockwise, that is, 0 is N, 90 is E, 180 is S, and 270 is W.

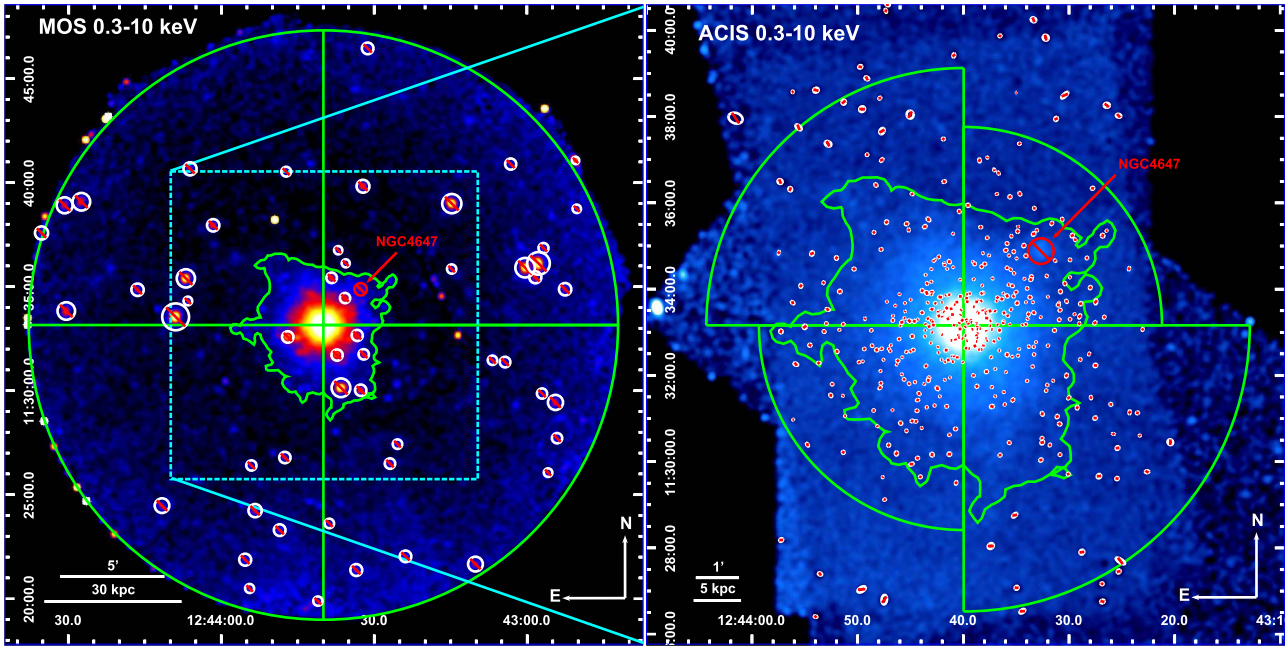

Figure 1. Left: *XMM*-MOS merged, exposure-corrected 0.3–10 keV image of NGC 4649. MOS1 and MOS2 data from ObsIDs 0021540201 (∼45 ks) and 0502160101 (∼70 ks) are reduced excluding intervals of high background flares and scaling the blank-sky files to match the high-energy count rate of the event files (Nevalainen et al. 2005). Point sources (marked with white circles) are detected on the merged event files with the sliding box method (EBOXDETECT), visually checked for spurious detections and indicated with white circles. The spectral extraction sectors used throughout the paper are shown in green, and the cyan dashed box represents the region expanded in the right panel. The green contours highlight the "stingray"-shaped large-scale emission from NGC 4649, with the faint wing-like structures reported by Woods et al. (2017) in the NE and SW directions. The location of the companion spiral galaxy NGC 4647 is indicated with a red circle. Right: same as the left panel, but for the *Chandra* ACIS merged, exposure-corrected 0.3–10 keV image. C6 and C7 data from ObsIDs 00785, 08182, 08507, 12975, 12976, and 14328 are reduced using the CGA pipeline, and the detected point sources are indicated with white ellipses.

data show a disturbed hot gas morphology on arcsecond scales, with similarity between X-ray emission and the Hα+[N II] features extending into the inner regions of the galaxy (Trinchieri & Goudfrooij 2002). Finoguenov et al. (2006), in their 2D spectral analysis of *XMM-Newton* data, found a number of ringlike enhancements in the iron abundance map, pressure disturbances in the central region, and large-scale entropy elongations associated with the regions of enhanced metallicity. An analysis of deeper *Chandra* data performed by Machacek et al. (2011) suggests gas sloshing on $\gtrsim$20 kpc scales (∼180″), showing spiral-like tails and multiple cold fronts, possibly caused by interaction with the companion spiral galaxy NGC 5850.

"Sloshing" may arise when a gas distribution initially close to HE is slightly offset by the interaction with a similar, separate system (e.g., the gravitational influence of a large galaxy falling through a galaxy group), causing oscillations of the ISM and the formation of arc-like cold fronts (e.g., Ascasibar & Markevitch 2006; ZuHone et al. 2010; Roediger et al. 2011; Lal et al. 2013). X-ray "bubbles" observed on sub-kiloparsec scale and coincident with radio emission suggest radio-mode feedback from the nuclear supermassive black hole. Machacek et al. also report ram pressure stripping of the companion elliptical galaxy NGC 5846A during its infall toward NGC 5846. X-ray mass profiles for this source have been produced by Das et al. (2008), combining the *XMM-Newton* gas profiles presented by Finoguenov et al. (2006) and long-slit SD data of Kronawitter et al. (2000) together with PN velocity dispersions presented by Coccato et al. (2008), and by Das et al. (2010), making use of the deprojected gas profiles obtained by Churazov et al. (2010) from *Chandra* and *XMM-Newton* data. The comparison between the azimuthally averaged Das et al. (2010) X-ray mass profile and the SLUGGS Survey SD–GC mass profile (Napolitano et al. 2014) shows that the X-ray mass profile falls below and above the optical profiles at distances smaller and larger than ∼10 kpc (∼90″), respectively, suggesting that the hot ISM is far from being in HE. We note that Ogorzalek et al. (2017) set lower limits on the turbulence velocities in the ISM of NGC 5846 too.

In Figure 4 we show the merged, exposure-corrected, broadband (0.3–10 keV) images of NGC 5846 from *XMM-Newton* MOS and *Chandra* ACIS in the left and right panels, respectively. The sectors used for the spectral extraction are indicated in green. Figure 5 shows the same data in the 0.3–2 keV band with different color scales to highlight small-scale (top panel) and large-scale (bottom panel) structures. The X-ray emission of NGC 5846 is clearly disturbed, showing the bubbles reported by Machacek et al. (2011) (see Figure 5, top right panel) related with the central active galactic nucleus (AGN) activity. In addition, edges in the NE and SW directions likely due to interaction with the group companion spiral galaxy NGC 5850 are evident, while in the NW direction the emission appears extended (see Figure 5, bottom panels). The surface brightness profiles presented in Figure 6 show in the NE (30–90) direction a clear perturbation corresponding to the cold front features reported by Machacek et al. (2011), while this effect is less evident in the other sectors. In Figure 6, we only show the NW (250–30) sector, where the gas is most

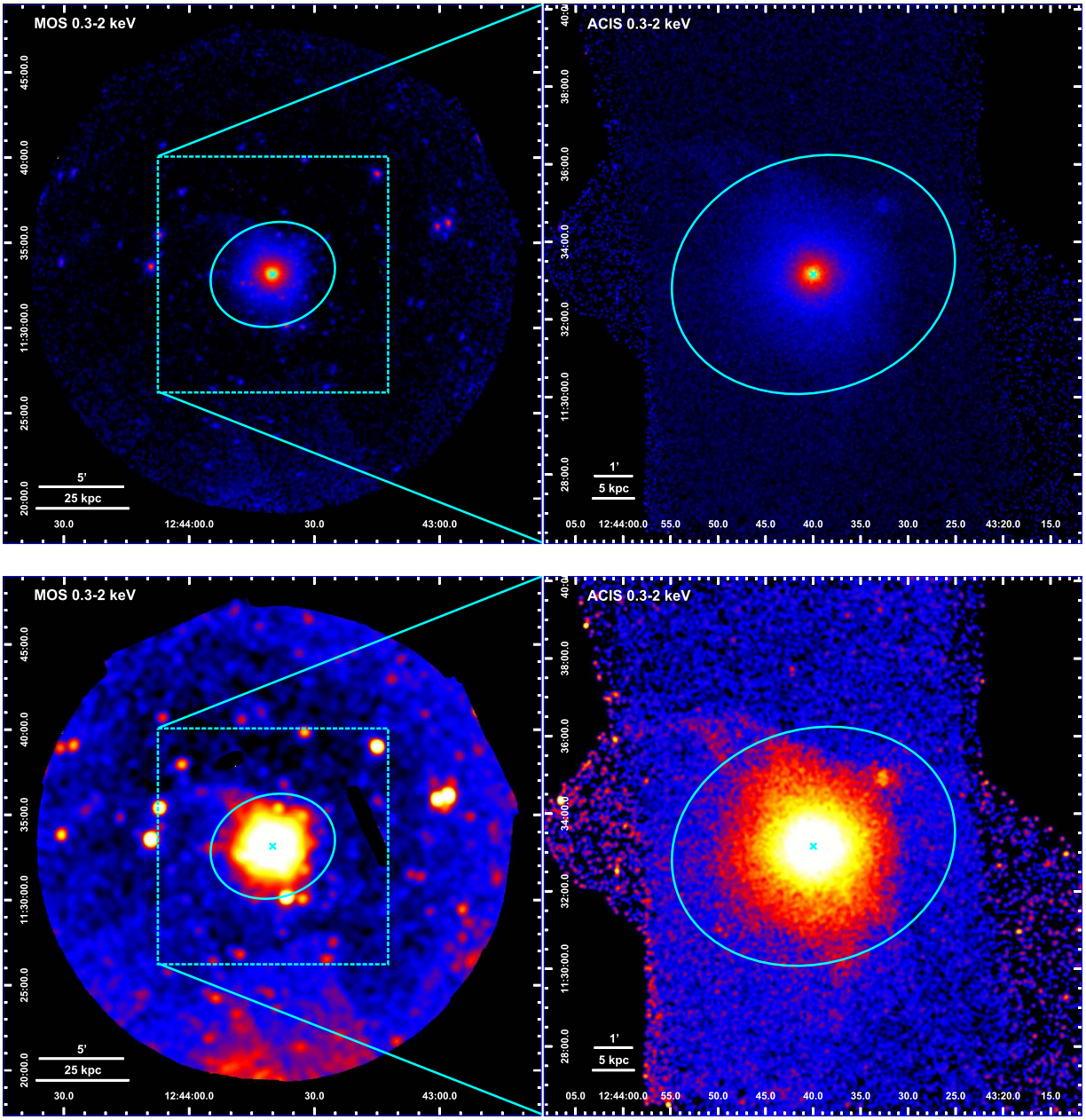

Figure 2. Same as Figure 1, but in the 0.3–2 keV band, with the D25 ellipse shown in cyan. Small-scale and large-scale structures are shown in top and bottom panels, respectively.

relaxed. The complete set of figures is presented in Appendix C.

3. Data Analysis

For our analysis we use both *Chandra* ACIS and *XMM-Newton* MOS data. The spatial resolution of ACIS reveals fine ISM features and disturbances in the inner regions of the galaxies. The large field of view (FOV) of EPIC-MOS allows us to extend the analysis to larger radii to constrain the ISM features in lower surface brightness regions.

3.1. Chandra Data

We make use of the *Chandra* ACIS data products of the *Chandra* Galaxy Atlas (CGA) project (D.W. Kim et al. 2017, in preparation). The CGA project aims at analyzing in a uniform way *Chandra* ACIS archival data from a sample of 100 ETGs to systematically study the 2D spectral properties of the diffuse emission. While we generally follow the CIAO science threads, we have developed our own analysis pipelines. Below we briefly describe the key steps in data reduction.

Once ACIS data are retrieved from the *Chandra* Data Archive,[7] we run the ACIS level 2 processing with CHANDRA_REPRO to apply up-to-date calibrations (CTI correction, ACIS gain, bad pixels). After excluding time intervals of background flares exceeding 3σ with the DEFLARE task, we obtain the low-background total exposures listed in Table 2. For each observation, we generate a full-resolution image in multiple energy bands. We then use WAVDETECT to detect point sources in each observation. Individual observations are

[7] http://cda.harvard.edu/chaser

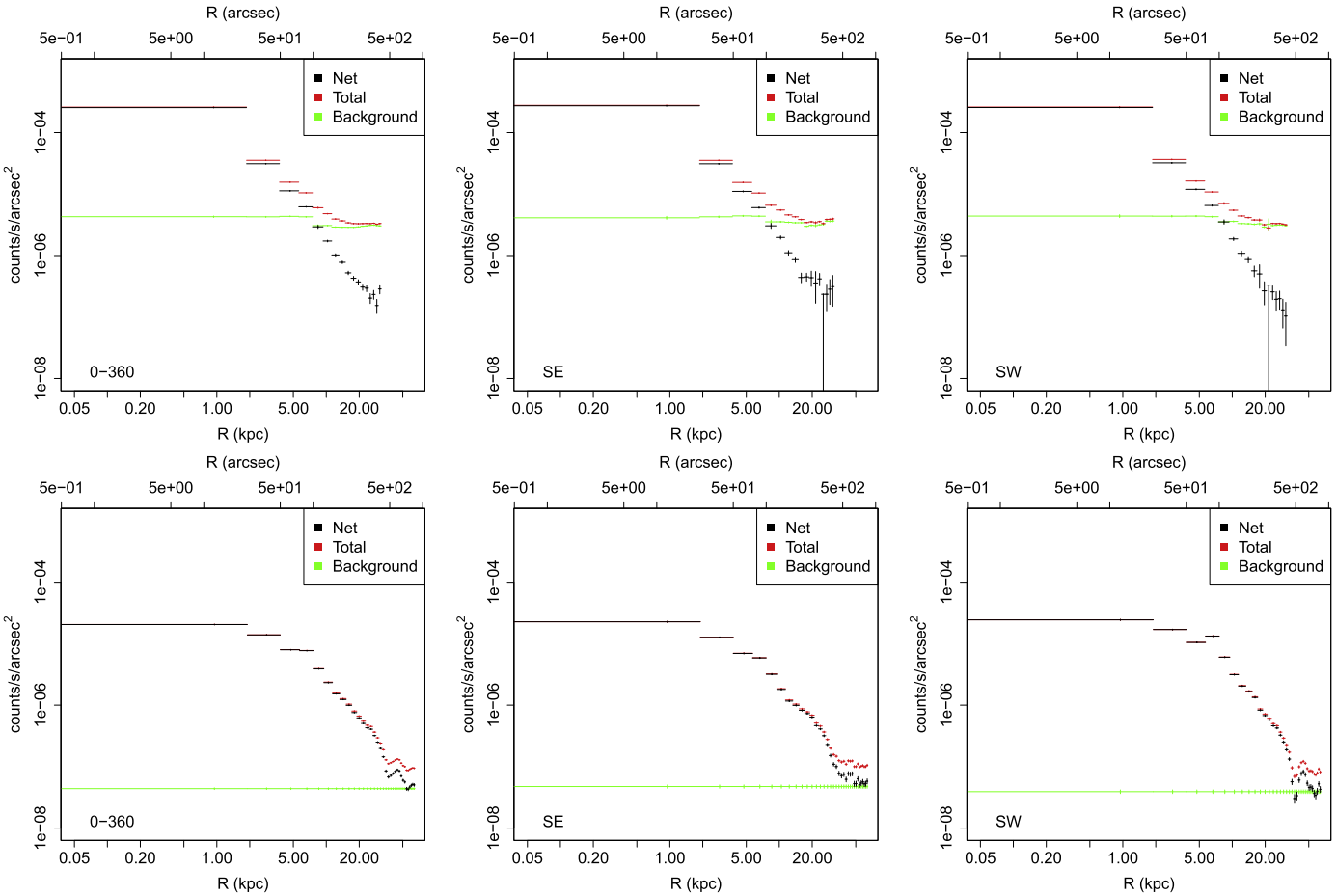

Figure 3. Brightness profiles for NGC 4649 in the 0.3–10 keV band in the different sectors shown in Figure 1, for (from left to right) full (0–360), SE (90–180), and SW (180–270), respectively. In particular, we show brightness profiles for *Chandra* ACIS data in the top row and for the *XMM*-MOS data obtained from the reduction procedure proposed by Nevalainen et al. (2005) in the bottom row. The annuli width is ∼25″, 50 pixels for *Chandra* ACIS data and 500 pixels for *XMM*-MOS data. Red, black, and green points represent total, net, and background brightness profiles, respectively.

corrected for a small positional inaccuracy by registering common sources (with REPROJECT_ASPECT), reprojected onto a single tangent plane (with REPROJECT_OBS) and merged into a single event file (with FLUX_OBS). We then run WAVDETECT for a second time to detect point sources from the merged images in 0.5–5 keV and remove them before extracting spectra.[8]

To estimate the background emission, we download the blank-sky data from the *Chandra* archive, reproject them to the same tangent plane as each observation (see Section 3.1), and rescale them to match the rate at higher energies (9–12 keV) where the photons are primarily from particle background (Hickox & Markevitch 2006).

3.2. XMM-Newton Data

EPIC data were retrieved from the *XMM-Newton* Science Archive[9] and reduced with the SAS[10] 14.0.0 software. To avoid cross-calibration problems and perform our analysis on as homogeneous data as possible, we restricted our analysis to MOS data. The main properties of the *XMM-Newton* data used in this work are presented in Table 3.

[8] In addition, data from the companion galaxy NGC 4647 (located at ∼2.′5 from NGC 4649 in the NW direction) were excluded for the present analysis.

[9] http://nxsa.esac.esa.int/nxsa-web

[10] http://www.cosmos.esa.int/web/xmm-newton/sas

3.2.1. Background Subtraction

Since one of the biggest sources of uncertainty in *XMM-Newton* data analysis is the background evaluation, we confronted three different ways of reducing MOS data. Here we briefly sum up the main properties of these methods, while a complete discussion of them can be found in Appendices A and B.4.

Simple Background Subtraction: Following the prescriptions of Nevalainen et al. (2005), the background is evaluated from appropriate blank-sky files, normalized to match the 9.5–12 keV count rate of the event files. However, since the particle background and the sky background are independent, we apply this normalization only in the 2–7 keV band. The main advantage of this background subtraction procedure is represented by its simplicity both in the data reduction and in the spectral fitting phases. In addition, it allows for spectral extraction over the whole MOS FOV. However, the use of blank-sky files represents an approximation over a complete background modeling and may not be accurate enough at surface brightness close to the background level.

Double Background Subtraction: The second reduction method is that proposed by Arnaud et al. (2001, 2002). To disentangle the cosmic X-ray background from the instrumental background, we made use of vignetting-corrected event files, since the cosmic X-ray background

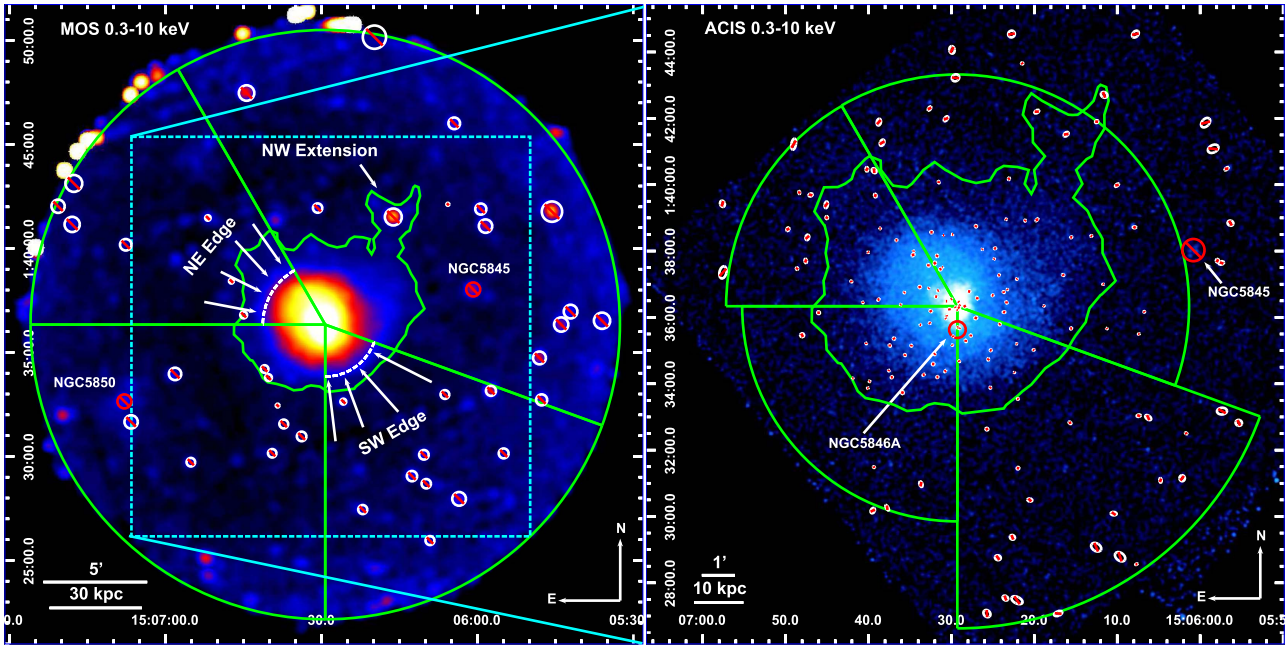

Figure 4. Left: *XMM*-MOS merged, exposure-corrected 0.3–10 keV image of NGC 5846. MOS1 and MOS2 data from ObsIDs 0021540501, 0723800101, and 0723800201 (∼165 ks) are reduced excluding intervals of high background flares and scaling the blank-sky files to match the high-energy count rate of the event files (Nevalainen et al. 2005). Point sources (marked with white circles) are detected on the merged event files with the sliding box method (EBOXDETECT) and visually checked for spurious detections. The spectral extraction sectors used throughout the paper are shown in white. The cyan dashed box represents the region expanded in the right panel. The green contours highlight the large-scale emission from NGC 5846, with the edges associated with the cold fronts reported by Machacek et al. (2011) in the NE and SW direction, as well as the extended emission in the NW sector. The location of the companion galaxies NGC 5845, NGC 5850, and NGC 5846A is indicated with red circles. Right: same as the left panel, but for the *Chandra* ACIS merged, exposure-corrected 0.3–10 keV image. C0, C1, C2, C3, C6, and C7 data from ObsIDs 00788 and 07923 (∼110 ks) are reduced using the CGA pipeline, and the detected point sources are indicated with white ellipses.

can be considered uniform on scales ∼30′ but is affected by vignetting, while the instrumental background is nonuniform but is not vignetted. We first subtracted from the source spectrum the spectrum extracted in the same region from the blank-sky file. Then we performed the same procedure, but from a region of the FOV that we *assumed* to be source free. Finally, we subtracted these two net spectra, taking into account the ratio of the extraction region areas. The resulting spectrum is expected to contain only source emission. This procedure yields a precise evaluation of the *XMM-Newton* background, being able to at least partially disentangle the astrophysical and the instrumental background. This, however, requires the selection of a source-free region.

Background Modeling: The third reduction method we adopted is the one proposed in the "Cookbook for Analysis Procedures for *XMM-Newton* EPIC Observations of Extended Object and the Diffuse Background"[11] (Snowden & Kuntz 2011). The background for this reduction method is partly subtracted and partly modeled. In addition, we modeled the instrumental and the cosmic background. This procedure allows us to analyze the whole MOS FOV, subtract the quiescent particle background (QPB), and model the instrumental and the cosmic background. This, however, requires a more complex spectral modeling, with several free parameters that make it difficult to find stable fitting convergence in unsupervised analysis procedures (especially in conjunction with 3D deprojection; see Section 3.3).

[11] https://heasarc.gsfc.nasa.gov/docs/xmm/esas/cookbook/xmm-esas.html

3.2.2. Common Reduction Steps

Regardless of the data reduction procedure adopted, the final steps we performed on the data sets were the same. In particular, we merged data from MOS1 and MOS2 detectors from all observations using the MERGE task, in order to detect the fainter sources that would not be detected otherwise. Sources were detected on these merged images following the standard SAS sliding box task EDETECT_CHAIN, which mainly consists of three steps: (1) source detection with local background, with a minimum detection likelihood of 8; (2) remove sources in step 1 and create a smooth background map by fitting a 2D spline to the residual image; (3) source detection with the background map produced in step 2 with a minimum detection likelihood of 10.

The task EMLDETECT was then used to determine the parameters for each input source by means of a maximum likelihood fit to the input images, selecting sources with a minimum detection likelihood of 15 and a flux in the 0.3–10 keV band larger than 10^{-14} erg cm^{-2} s^{-1} (assuming an energy conversion factor of 1.2×10^{-11} cts cm^2 erg^{-1}). An analytical model of the point-spread function (PSF) was evaluated at the source position and normalized to the source brightness. The source extent was then evaluated as the radius at which the PSF level equals half of the local background. We finally visually inspected the detected sources and removed evident spurious detections (i.e., at chip borders, in regions of diffuse emission, etc.). We then produced "swiss-cheese" images for each detector array and observation.

3.3. Spectral Analysis

We extracted data for spectral analysis from circular annuli spanning an entire 360° or partial annuli with specific sectors,

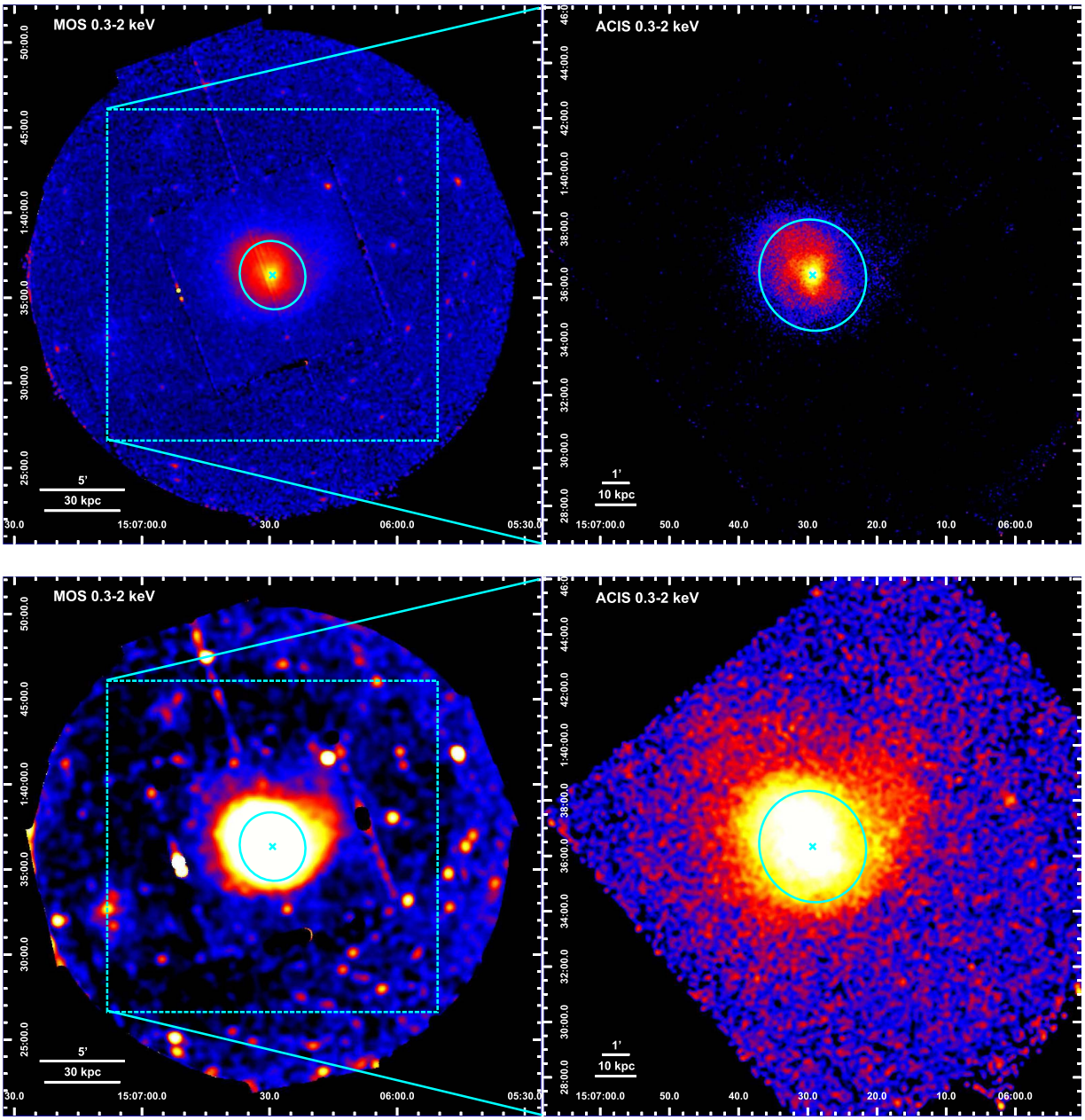

Figure 5. Same as Figure 4, but in the 0.3–2 keV band with the D25 ellipse shown in cyan. Small-scale and large-scale structures are shown in the top and bottom panels, respectively.

when the gas distribution was not spherically symmetric. The minimum width of each annulus was chosen to avoid the significant PSF scattering leading to strong mixing between the spectra in adjacent annuli. In particular, for *Chandra* ACIS we have chosen a minimum annulus width of 2 pixels (corresponding to about 1″), while for *XMM*-MOS we have chosen a minimum annular width of 600 pixels (corresponding to about 30″). In this way we obtained a finer grid in the inner regions of the galaxy with *Chandra* data, while we were able to extend to larger radii with *XMM-Newton* data.

The inner and outer radii of each annulus were adaptively determined, based on a given signal-to-noise ratio. In particular, we produced bins corresponding to minimum signal-to-noise ratios of 30, 50, and 100, for both *Chandra* and *XMM-Newton* data (the signal-to-noise ratio used for *XMM-Newton* and *Chandra* data is reported in the captions of Figures 7 and 10). If the selected signal-to-noise ratio could not be reached, the last spectral extraction bin was extended to the edge of the detector. For *Chandra* ACIS data the background is evaluated from blank-sky files (see Section 3.1). For *XMM*-MOS data the background has been evaluated using the prescriptions described in Sections 3.1 and 3.2.[12]

The source spectra were extracted from each spatial bin, in each observation. The corresponding arf and rmf files were also extracted per observation to take into account time- and position-dependent ACIS and MOS responses. Once source spectrum, background spectrum, arf, and rmf per ObsID were

[12] Note that for the reduction procedure presented in Snowden & Kuntz (2011) the background contribution cannot be estimated before the spectral fitting. Therefore, for this method we used the annuli obtained from the reduction method proposed by Nevalainen et al. (2005).

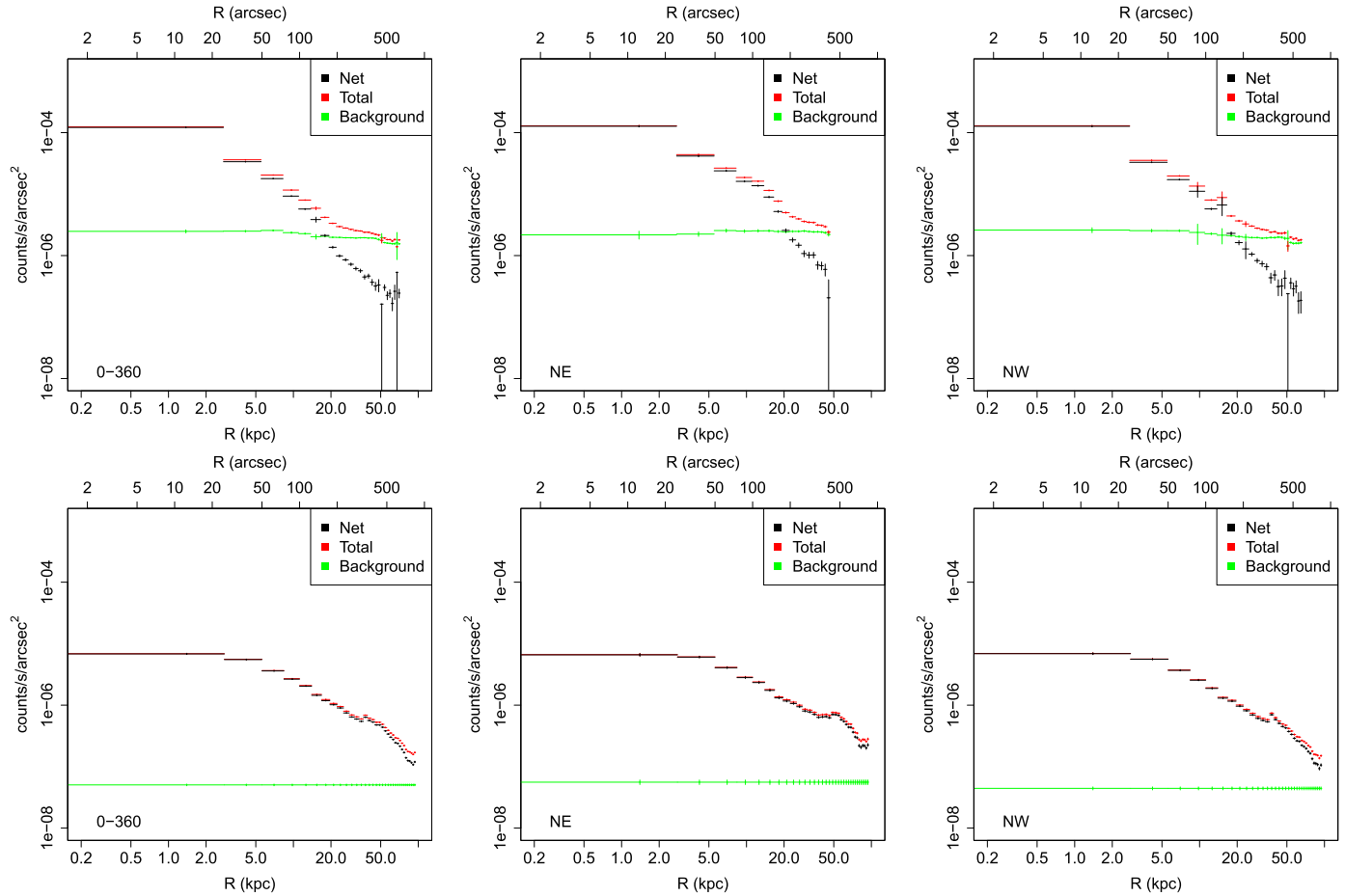

Figure 6. Brightness profiles for NGC 5846 in the 0.3–10 keV band in the different sectors shown in Figure 4, for (from left to right) full (0–360), NE (30–90), and NW (250–30), respectively. In particular, we show brightness profiles for *Chandra* ACIS data in the top row and for the *XMM*-MOS data obtained from the reduction procedure proposed by Nevalainen et al. (2005) in the bottom row. The annuli width is ∼25″, 50 pixels for *Chandra* ACIS data and 500 pixels for *XMM*-MOS data. Red, black, and green points represent total, net, and background brightness profiles, respectively.

Table 2
Summary of *Chandra* Data Used in This Work

(1) Source Name	(2) ObsID	(3) Obs. Date	(4) Array	(5) Exposure (ks)
NGC 4649	00785	2000 Apr 20	ACIS-S 6	34.6
			ACIS-S 7	22.2
	08182	2007 Jan 30	ACIS-S 6	48.3
			ACIS-S 7	47.0
	08507	2007 Feb 01	ACIS-S 6	15.0
			ACIS-S 7	17.3
	12975	2011 Aug 08	ACIS-S 6	80.9
			ACIS-S 7	77.3
	12976	2011 Feb 24	ACIS-S 6	99.2
			ACIS-S 7	98.2
	14328	2011 Aug 12	ACIS-S 6	13.2
			ACIS-S 7	14.0
NGC 5846	00788	2000 May 24	ACIS-S 6	22.2
			ACIS-S 7	23.2
	07923	2007 Jun 12	ACIS-I 0	87.5
			ACIS-I 1	88.2
			ACIS-I 2	88.0
			ACIS-I 3	88.2

Note. (1) Source name. (2) ObsID. (3) Observation date. (4) ACIS Array and chip used for the observation. (5) Clean exposure times after excluding time intervals of strong background flares.

Table 3
Summary of *XMM-Newton* Data Used in This Work

(1) Source Name	(2) ObsID	(3) Obs. Date	(4) Array	(5) Exposure (ks)
NGC 4649	0021540201	2001 Jan 02	MOS1	45.3/50.5/45.5
			MOS2	45.3/50.3/45.9
	0502160101	2007 Dec 19	MOS1	71.0/73.2/68.4
			MOS2	71.0/72.5/68.6
NGC 5846	0021540501	2001 Aug 26	MOS1	13.4/15.4/13.3
			MOS2	13.4/15.7/13.2
	0723800101	2014 Jan 21	MOS1	69.6/77.8/65.9
			MOS2	70.6/79.3/67.7
	0723800201	2014 Jan 17	MOS1	84.7/87.6/83.0
			MOS2	86.0/87.6/84.0

Note. (1) Source name. (2) ObsID. (3) Observation date. (4) MOS array used for the observation. (5) Clean exposure times for the reduction procedures described in Appendices A.1, A.2, and A.3.

generated, we used COMBINE_SPECTRA CIAO and EPICSPECCOMBINE SAS tools to create a single data set per each extraction bin. This way the spectral fitting is simpler and quicker. We compared our results with those of joint fitting of individual spectra and found no significant difference.

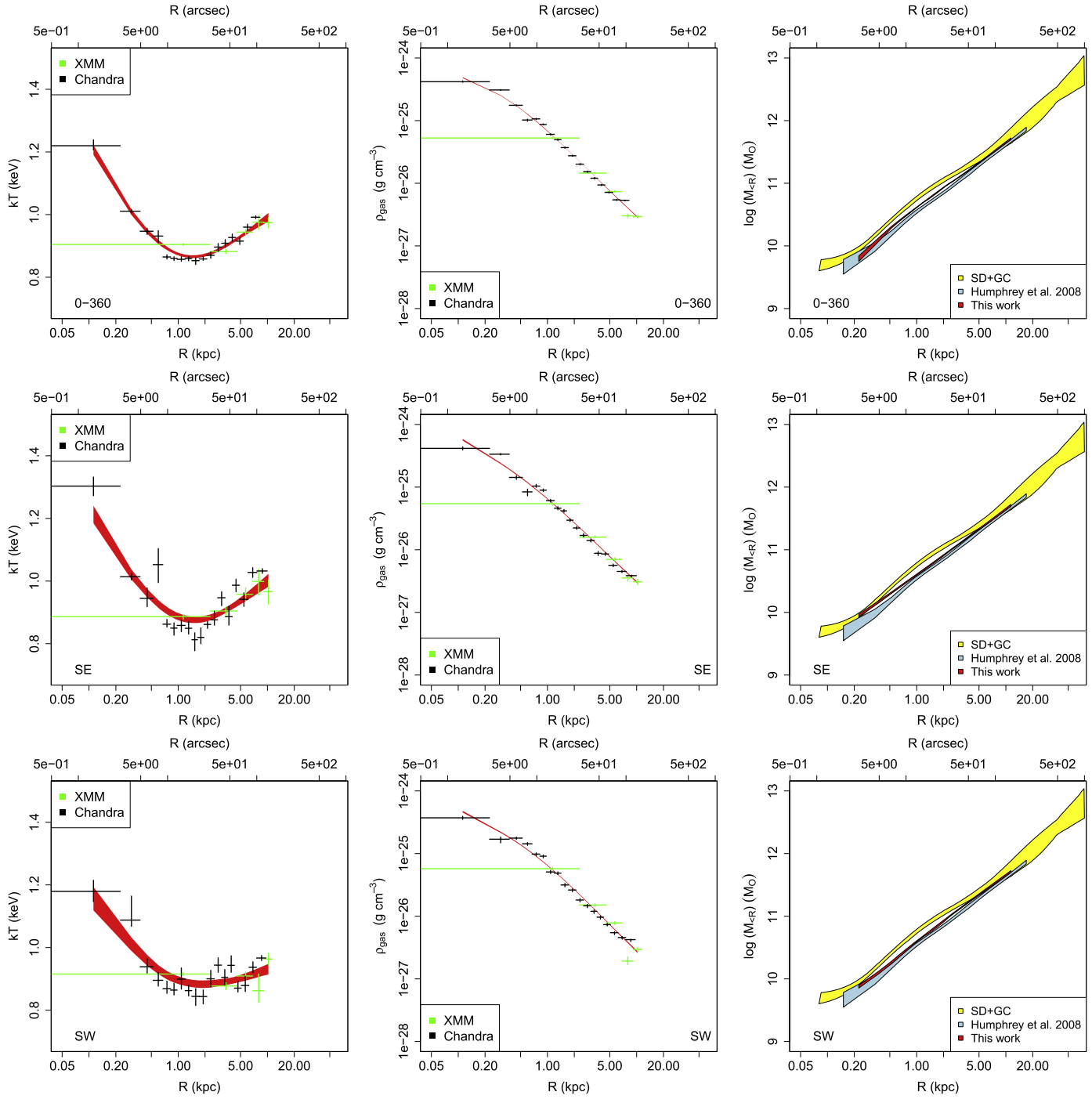

Figure 7. Gas profiles obtained in NGC 4649 with the reduction procedure proposed by Nevalainen et al. (2005). From top to bottom we show the profiles obtained in the full (0–360), SE (90–180), and SW (180–270) sectors, respectively. Spectra extracted in the annuli are then simultaneously fitted (separately for *XMM* and *Chandra* data) with the fixed abundance model and deprojected using the PROJCT model. The annuli width is chosen to reach a signal-to-noise ratio of 30 for *XMM*-MOS data (represented in red) and of 50 for *Chandra* ACIS data (represented in black), with the exception of the full (0–360) sector, for which we chose a signal-to-noise ratio of 50 for *XMM* data and 100 for *Chandra* data. Best fits of a smooth cubic spline are presented in red, with smoothing parameter from top to bottom of 0.7, 0.8, and 0.8. In each row we show the gas temperature (first column) and density (second column) profiles. In the third column we present in red the total mass profiles obtained by means of Equation (1) from the best fits to gas temperature and density profiles. In the same panels we show in yellow the optical mass profile obtained from SD and GC reported by Shen & Gebhardt (2010) and in light blue the X-ray mass profiles obtained by Humphrey et al. (2008).

To make use of the χ^2 fit statistic, we binned the spectra to obtain a minimum of 20 counts per bin using the SPECEXTRACT and EVSELECT tasks; in the following, errors correspond to the 1σ confidence level for one interesting parameter ($\Delta\chi^2 = 1$). In all the spectral fits we included photoelectric absorption by the Galactic column density along the line of sight reported in Table 1. To account for projection effects, we used the PROJCT model implemented in XSPEC (ver. 12.9.0o; Arnaud 1996) excluding data from any detected point source.

Spectral fitting was performed separately for *Chandra* and *XMM-Newton* data in the 0.5–8 keV energy range, adopting Gehrels weighting (Gehrels 1986), and using a model comprising

a APEC thermal component (with solar abundances from Grevesse & Sauval (1998) and ATOMDB code v2.0.2[13]) plus a thermal bremsstrahlung component with temperature fixed at 7.3 keV to account for undetected point sources (Irwin et al. 2003). In order to obtain stable fits, we first performed 2D projected fits to get reliable starting values for the 3D deprojected profiles, and then we applied the PROJCT model; after fitting these profiles, we froze the bremsstrahlung component normalizations to their best-fit values to reduce the uncertainties on the more relevant parameters of our analysis.

Since the outermost (and usually larger) spectral extraction bin does not reach the minimal signal-to-noise requirement, its spectral parameters are usually not well constrained and show large fluctuations. Moreover, due to the "onion peeling" procedure used in the 3D deprojected process, this outermost bin influences all the inner shells and may yield unreliable results. To avoid this problem, we excluded the outermost bin from the following analysis and only considered bins that reach the selected minimum signal-to-noise ratio. Regarding the APEC component metal abundances, we performed spectral fits both linking the abundances between all sectors (*fixed* abundances) and allowing the element abundances to freely vary in each annulus (*free* abundances). In the latter case, however, we usually had to use binning with higher signal-to-noise ratio in order to be able to constrain the element abundances. We note that in general we conservatively choose the same signal-to-noise ratio for both the fixed and free abundance models to compare the resulting profiles on the same grounding, while as a general rule the fixed abundance models can be pushed to lower signal-to-noise ratios. Uncertainties on best-fit parameters (APEC component temperatures, normalizations, and element abundances) were then evaluated with the ERROR command, and finally we converted the APEC normalizations EM to the gas density ρ using the relation $\rho = \sqrt{\mathrm{EM} \cdot 10^{14}/\eta \cdot V \cdot 4\pi[(1+z)\cdot D_A]^2}$, where η is the electron-to-hydrogen ratio (which we assume to be 1.2 for a fully ionized gas), V is the volume of the elliptical shell, z is the source redshift, and D_A is the angular diameter distance to the source. From the gas temperature (T) and density (ρ) profiles we then produced gas pressure $P = k\ T\ n$ and entropy $S = kT/n^{2/3}$, where k is the Boltzmann constant, m_p is the proton mass, $\mu \approx 0.62$ is the average molecular weight factor, and $n = \rho/(\mu\ m_p)$ is the gas number density.

3.4. X-Ray HE Mass Profiles and Gas Profile Fitting

From the gas temperatures T and density ρ profiles that we obtain in the various sectors, we can evaluate the total mass profiles under the assumption of HE:

$$M(<R) = -R\,\frac{kT(R)}{G\mu m_p}\left(\frac{d\log\rho}{d\log R} + \frac{d\log T}{d\log R} + \frac{P_{\rm NT}}{P}\frac{d\log P_{\rm NT}}{d\log R}\right), \quad (1)$$

where $P_{\rm NT}$ is the nonthermal pressure component. All the X-ray mass profiles presented in the following analysis are obtained assuming $P_{\rm NT} = 0$. To make use of the HE equation, we need to model $T(R)$ and $\rho(R)$ to have a good estimate of the (logarithmic) slopes that go into Equation (1). While broken or double-broken power laws have been used (e.g., Humphrey et al. 2008), for this work we decided to fit the gas profiles with a cubic smoothing spline (SMOOTH.SPLINE R language package; see, e.g., Johnson et al. 2009), to avoid sudden variations in the profile slopes and so in the resulting mass profiles. This spline function's smoothing parameter (typically in the 0–1 range) can be varied, with 0 yielding the interpolating spline and 1 yielding a monotone fit to the data. Fit models for gas pressure and entropy profiles were performed by combining fit models for the gas temperature and pressure profiles as indicated in Section 3.3.

For each sector we fitted the merged *Chandra* ACIS and *XMM-Newton* MOS profiles with a cubic spline with increasing smoothing parameter from 0.5 to 1.0. To evaluate the uncertainties on the best-fit function, we performed Monte Carlo simulations drawing from the observed temperature and density distributions assuming a Gaussian distribution. To take into account the asymmetric error bars that we get from the spectral fittings, we considered two Gaussian distributions with different widths—for the upper and lower errors—and drew for each of them 1000 random realizations of the profiles, which were then fitted with the cubic spline. From these results we then evaluated the distribution of the best-fit functions and of their slopes. We add that, at variance with the standard practice of producing mass profile points at the central radius of each bin, we instead decided to produce the mass profile points at the outermost radii of each bin. This is due to the fact that our main goal in this work is to estimate the DM distribution, which is better constrained at the largest radii. Finally, we notice that for NGC 4649 we also tried including in the spectral fitting an additional hot gas component, with temperature fixed at 2.5 keV (e.g., Gastaldello & Molendi 2002), to account for possible interloper emission from the Virgo Cluster, but we did not find any significant effect of this additional model component on the final mass profiles.

3.5. Factors Affecting the HE Mass Profiles

In producing the total HE mass profile, there are a number of effects that must be taken into account, namely, the smoothing parameter of the spline function used to fit the gas density and temperature profiles, the different angular sections when the hot gas distribution is not azimuthally symmetric, the radial gradient of metal abundances, and the accuracy in background subtraction. These effects are discussed in detail in Appendix B. Here we briefly sum up the main aspects of our assumptions.

1. Low values of the smoothing parameter of the spline function yield best-fit models catching the finer details of the gas profiles, while large values of the smoothing parameter favor monotonic profiles. The choice of the smoothing parameter value is a trade-off between the fit function ability to represent the details of the gas profiles and the need to get rid of the noise to get meaningful physical results. In general, we choose a value of the smoothing parameter between 0.6 and 0.8 (see captions of Figures 7 and 10).
2. The total HE mass obtained from Equation (1) is the total mass enclosed within a radius R assuming spherical symmetry, that is, the total mass assuming that the gas is in HE and distributed in a spherical shell with constant

[13] http://www.atomdb.org

temperature. Therefore, even if we extract spectra in angular sectors, it will make sense to compare the resulting mass profiles with each other and with the mass profiles from optical markers.

3. Although the abundance profiles are rather noisy, they tend to decrease at larger radii, and this yields flatter gas density profiles and therefore smaller enclosed mass. Allowing variable abundances yields in addition larger uncertainties (especially on gas density), which in turn translates to larger uncertainties on the enclosed mass profile.
4. The different background subtraction methods yield similar gas and mass profiles, with only minor effects on the outer bins at fainter surface brightnesses. For the double subtraction method, however, we have to assume a source-free region that will be excluded by our spectral extraction, so the main effect of the background subtraction proposed by Arnaud et al. (2001, 2002) is to restrict our analysis to smaller radii in certain directions. In the following, therefore, we will focus on results from Nevalainen et al.'s procedure.

4. Results

4.1. NGC 4649

We extracted spectra and HE mass profiles in the four quadrant directions NW (270–360), NE (0–90), SE (90–180), and SW (180–270). As mentioned in Section 2, for this source we restrict our analysis to the inner 12 kpc region in order to avoid the disturbed regions reported by Woods et al. (2017). On sub-kiloparsec scales the NE and SW quadrants contain the weak radio jet (Condon et al. 2002) emerging from the central faint AGN, as well as the associated cavities in the X-ray-emitting gas, while in the NW and SE quadrants lie the overdense regions where the gas is displaced on the sides of the jet (Paggi et al. 2014).

In Figure 7 we show the gas profiles (temperature and density) in the full 360 sector (top row), in the SE (middle row), and in the SW (bottom row) obtained with *Chandra* (black) and *XMM-Newton* data (green). The complete set of gas and mass profiles is presented in Appendix C. These gas profiles are obtained with the fixed abundance model. In the same figures, we overplot the best-fit models to these profiles in red, with the width of the curve indicating the corresponding 1σ error. In the third column of the same figure we show the total HE mass profiles (in black) obtained in the various sectors by means of Equation (1) from the best fits to gas temperature and density profiles. In the same panels these HE mass profiles are compared with the mass profile (in yellow) obtained from SD and GC kinematics (Shen & Gebhardt 2010). We also compare our HE mass profiles with the HE mass profiles (in light blue) obtained by Humphrey et al. (2008) making use of *Chandra* data. In Figure 8 we show the gas profiles obtained with the free abundance model together with the total HE mass profiles obtained from the best fits to gas temperature and density profiles. In addition, in the rightmost panels of the same figure we show the element abundance profiles in comparison with the fixed abundance model.

Our HE mass profiles in different sectors (at $R = 3$–12 kpc) are all relatively similar, consistent with the optical measurement, and confirm the relaxed morphology of the ISM in NGC 4649 at these scales, without evidence for strong azimuthal asymmetry. The NE sector has the largest masses in the radius range of 0.5–3 kpc, almost consistent with the optical measurement at the same radius, while the SW sector has the lowest masses, most significantly discrepant from the optical measurement. The uncertainties in the small-scale HE mass profiles, as reflected by the range of mass profiles among different sectors, could have a significant impact when X-ray data are used to estimate the mass of the nuclear supermassive black hole (see Section 4.3).

The discrepancies between the optical and the X-ray HE mass profiles indicate deviations from the HE between 0.5 and 3 kpc and confirm the nonthermal pressure component accounting for $\sim$30% of the observed gas pressure as reported by Humphrey et al. (2008) and Paggi et al. (2014).

The X-ray HE mass profiles of Humphrey et al. (2008) were obtained with a VAPEC component to model the ISM emission with free abundances, so they are closer to our HE mass profiles obtained with the free abundance model. However, Humphrey et al. used a broken power law for modeling the gas profiles, which might explain the minor differences from our results (see third column in Figure 7). In addition, Humphrey et al. made use of ATOMDB v1.3.2, which yields systematically lower temperatures with respect to v2.0.2 in the temperature range of interest here (see Loewenstein & Davis 2012).

These differences are highlighted in the velocity profiles (as evaluated from $v = \sqrt{(GM_X/R)}$) presented in Figure 9, where in the left and right panels we show HE profiles from fixed and free abundance models, respectively, and compare them with those of Humphrey et al. (2008), the velocity profile of Shen & Gebhardt (2010), and the measurement of Alabi et al. (2016) at $5R_e$ (25 kpc). In the same figure we show the velocity profile from Das et al. (2011) that best fits their SD, GC, and PN data. This profile follows Shen & Gebhardt's up to 7.6 kpc and is flat from that point onward (their VC4 profile); it is compatible with Alabi et al.'s point, as well as with our X-ray HE profiles. In this figure the uncertainties on the velocity profiles obtained in this work are not shown, and the width of these profiles is fixed for clarity of representation (proper errors are presented in Figures 7 and 8).

4.2. NGC 5846

To investigate the effects of azimuthally asymmetric gas morphology on HE mass profiles, we extracted spectra in four sectors in the NE (30–90), SE (90–180), SW (180–250), and NW (250–30), directions, as well as in the full (0–360) sector (see Figures 4 and 5). The NE and SW sectors are the most disturbed since they contain a surface brightness edge (Machacek et al. 2011), while the SE sector shows a smaller amount of disturbance. Machacek et al. (2011) suggest that these features may result from interactions with group galaxies. In the NW sector instead the gas emission appears extended, smooth, and mostly relaxed.

In Figure 10 we show the gas profiles obtained with fixed element abundances from the Nevalainen et al. (2005) reduction process for the *XMM-Newton* data. Profiles are in the full (0–360) sector and in the NW and NE directions, representative of the most disturbed and most relaxed ISM conditions (the complete set of gas and mass profiles is presented in Appendix C). In Figure 11 we show the gas profiles obtained in the different sectors but with the free

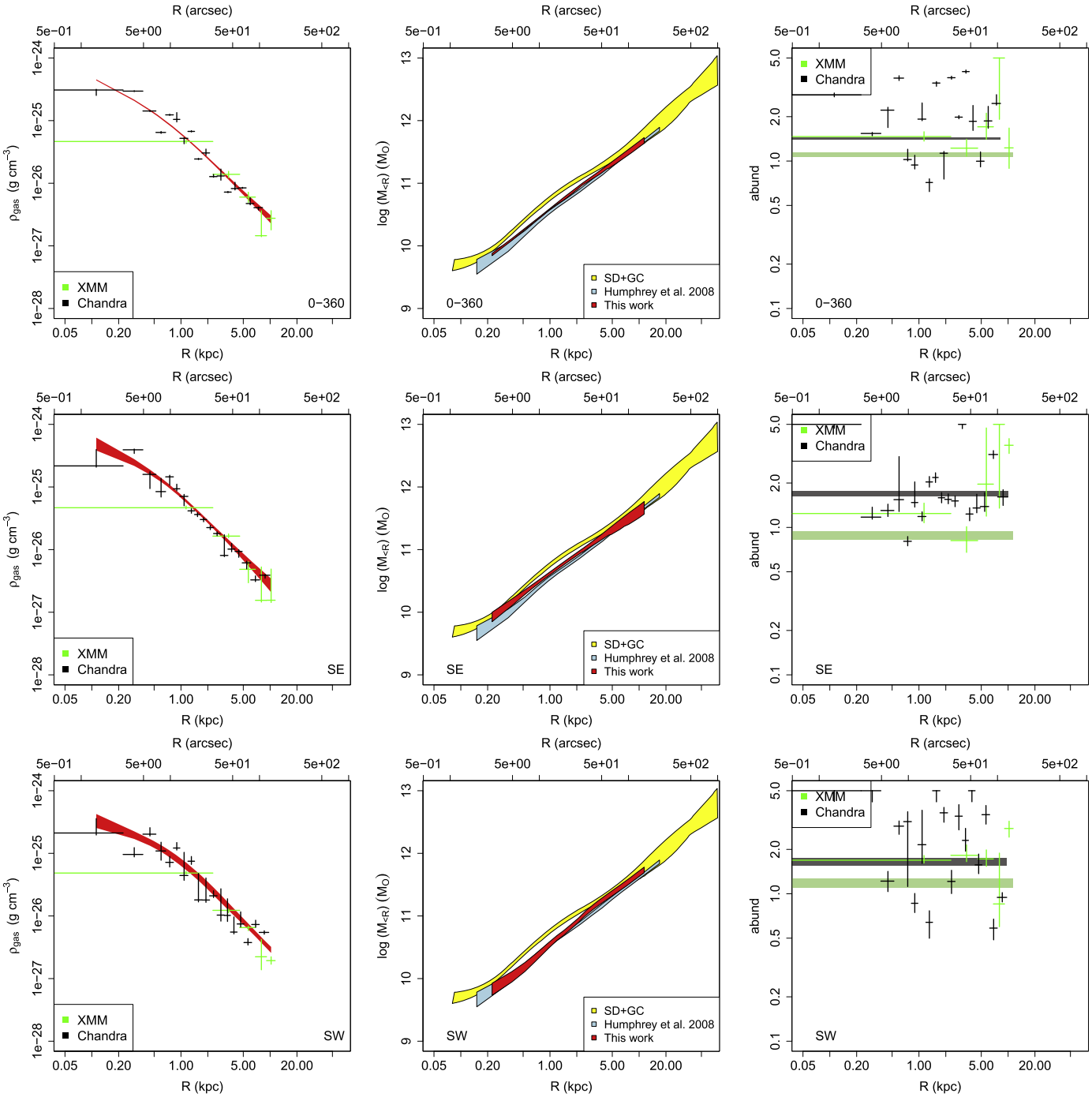

Figure 8. Same as Figure 7, but with the free abundance model (temperature profiles are similar to the fixed abundance model case and therefore omitted). In addition, on the rightmost panel of each row we show the element abundance profiles for *XMM*-MOS data (in green) and for *Chandra* ACIS data (represented in black). In the same panels we overplot with green and black rectangles the values of the element abundances obtained with the fixed abundance model for *XMM* and *Chandra* data, respectively.

abundance model. We also compare our mass profiles with the optical mass profile (in yellow; Napolitano et al. 2014), which makes use of SD and GC kinematics from the SLUGGS Survey, and with the X-ray mass profile (in light blue) previously determined by Das et al. (2010) from *Chandra* and *XMM-Newton* data. Again, we highlight these differences in the velocity profiles presented in Figure 12, where in the left and right panels we show HE X-ray profiles from fixed and free abundance models, respectively, and compare them with the HE X-ray profile of Das et al. (2010), the mass profile of Napolitano et al. (2014), and the mass measurement at $5R_e$ (33 kpc) by Alabi et al. (2016). The uncertainties on the velocity profiles obtained in this work are not shown, and the width of the latter is fixed for clarity of representation (proper errors are presented in Figures 10 and 11). A comprehensive mass analysis of NGC 5846 that includes SD, GC, and also PN data has been recently presented by Zhu et al. (2016), yielding profiles close to those of Napolitano et al.

The X-ray HE mass profiles of Das et al. (2010) were obtained with element abundances fixed to 0.5 solar, and as

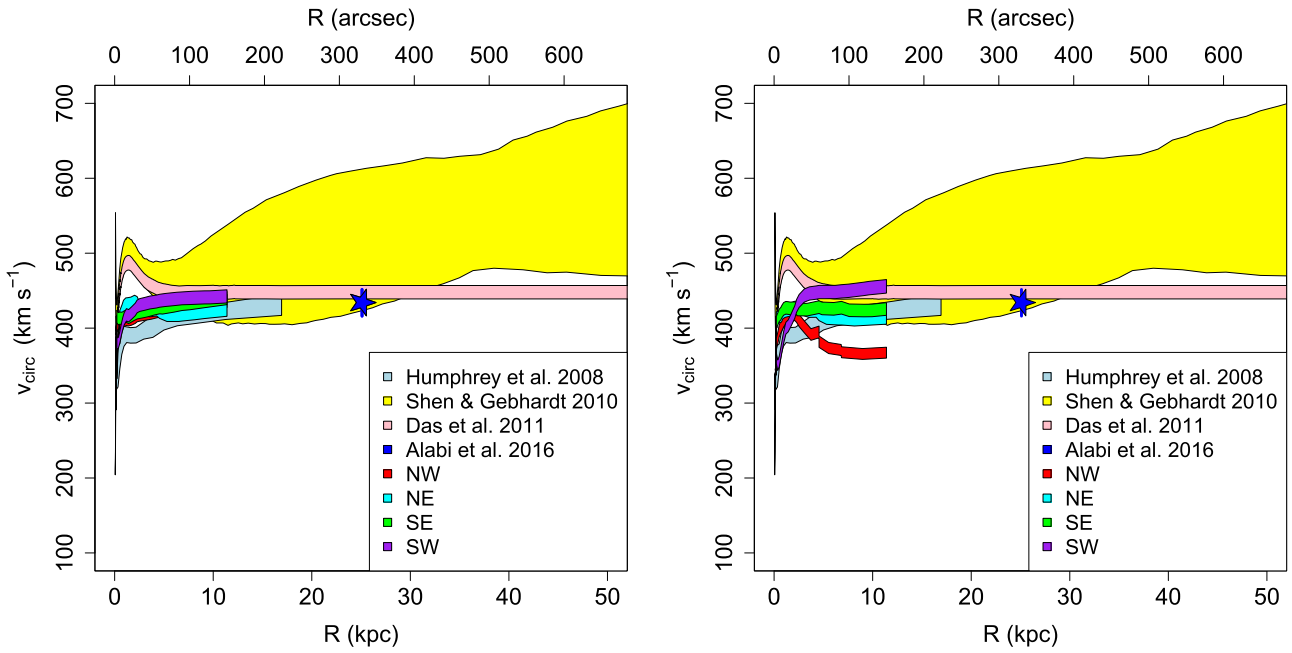

Figure 9. Left: comparison of velocity profiles of NGC 4649 from fixed abundance models. The profiles for different angular sectors are shown in different colors indicated in the legend, while the X-ray profile presented by Humphrey et al. (2008) is shown in light blue, the SD+GC profile presented by Shen & Gebhardt (2010) is shown in yellow, the profile from Das et al. (2011) obtained with X-ray and PN data is presented in pink, and the blue star represents the measurement by Alabi et al. (2016), with the corresponding uncertainty shown with a vertical blue line. Right: same as the left panel, but for free abundance models.

expected, are closer to our fixed abundance profiles than our free abundance profiles. Also, the HE mass profile of Das et al. extends down to ∼0.8 kpc, while ours stops at ∼1.6 kpc because, as explained in Section 3.4, our HE mass profiles are evaluated at the outer radius of each bin rather than at its center. At the central region ($R < 10$ kpc), the X-ray HE profiles lie below the optical profile. This discrepancy is seen in all sectors. As in the central region of NGC 4649, we interpret these small-scale deviations from optical profiles as ISM disturbances (e.g., cavities) in the inner regions of the galaxy connected with recent AGN activity (Machacek et al. 2011).

As noted by Napolitano et al. (2014), the Das et al. (2010) HE mass and velocity profiles fall below and above the optical profiles at distances smaller and larger than ∼15 kpc, respectively, thus indicating that the ISM in this source deviates from HE. When looking at the fixed abundance models, we could reproduce the similar discrepancies in the NE sector (third column in the second row of Figure 10). We interpret the deviations of the X-ray mass profiles from the optical one as a consequence of environmental effects, possibly due to sloshing of the hot ISM in NGC 5846 caused by the interaction with the group companion NGC 5850, compressing and decompressing the gas for $R \geqslant 15$ kpc and $R \leqslant 15$ kpc, respectively; in fact, a discrepancy with a mass jump similar to that shown here has been found in A1795, considered a typical example of sloshing in galaxy clusters (Markevitch et al. 2001). In the NW sector (the last column in the top row) where the hot gas is most relaxed, our HE mass profile is smooth (the circular velocity increases slowly but monotonically) and close to the optical mass profile. However, the X-ray mass profile is still higher than the optical profile even in the NW sector. When allowing for variable element abundances, the large-scale deviations between X-ray- and optical-derived mass profiles considerably decrease. This is because the negative abundance gradient (decreasing with increasing radii; see the last column in Figure 11) effectively reduces the pressure gradient, resulting in flatter mass profiles (see also Figures 24 and 25). In particular, in the NW sector (the third column in the bottom row), the HE X-ray mass profile from the free abundance model is consistent with the optical profile.

4.3. Total Mass

To assess the effect of the deviation from HE on the X-ray measurement of total mass, we compare our results with those of SLUGGS (Alabi et al. 2016). We adopt their values for R_e and measure the mass within five effective radii (roughly corresponding to the limit of optical mass tracers; Deason et al. 2012; Alabi et al. 2016). At $5R_e$ DM should also dominate the total mass.

The HE masses from different sectors are summarized in Table 4, with the maximum radius $R_{\rm max}$ reached in the present analysis (column (3)), the R_e values from Alabi et al. (2016) (column (4)), and the total mass M_X enclosed in $5R_e$ (column (5)) for both fixed and free element abundance models. If $R_{\rm max}$ does not reach $5R_e$ because of signal-to-noise ratio limitations (see Section 3.3) or because it exceeds the 12 kpc boundary imposed to exclude the Virgo ICM and regions affected by ram pressure effects (Woods et al. 2017), we extrapolate to this radius the mass profile fitting presented in Section 4.4 and indicate the value of $M_X(<5R_e)$ with an asterisk. The value of $M_X(<5R_e)$ in boldface is the one that we consider reliable, and it is derived from the NW sector of NGC 5846 where we do not find strong deviations from HE from comparison with the optical mass profiles. This value is based only on X-ray data and does not depend on any particular assumed model for the DM halo.

We compare our results with the total mass enclosed in $5R_e$ as extrapolated from previous X-ray studies (column (6); Humphrey et al. (2008) for NGC 4649 and Das et al. (2010) for NGC 5846), and with the total mass M_O enclosed in $5R_e$ from kinematic estimates (columns (7) and (8); compare Alabi et al.

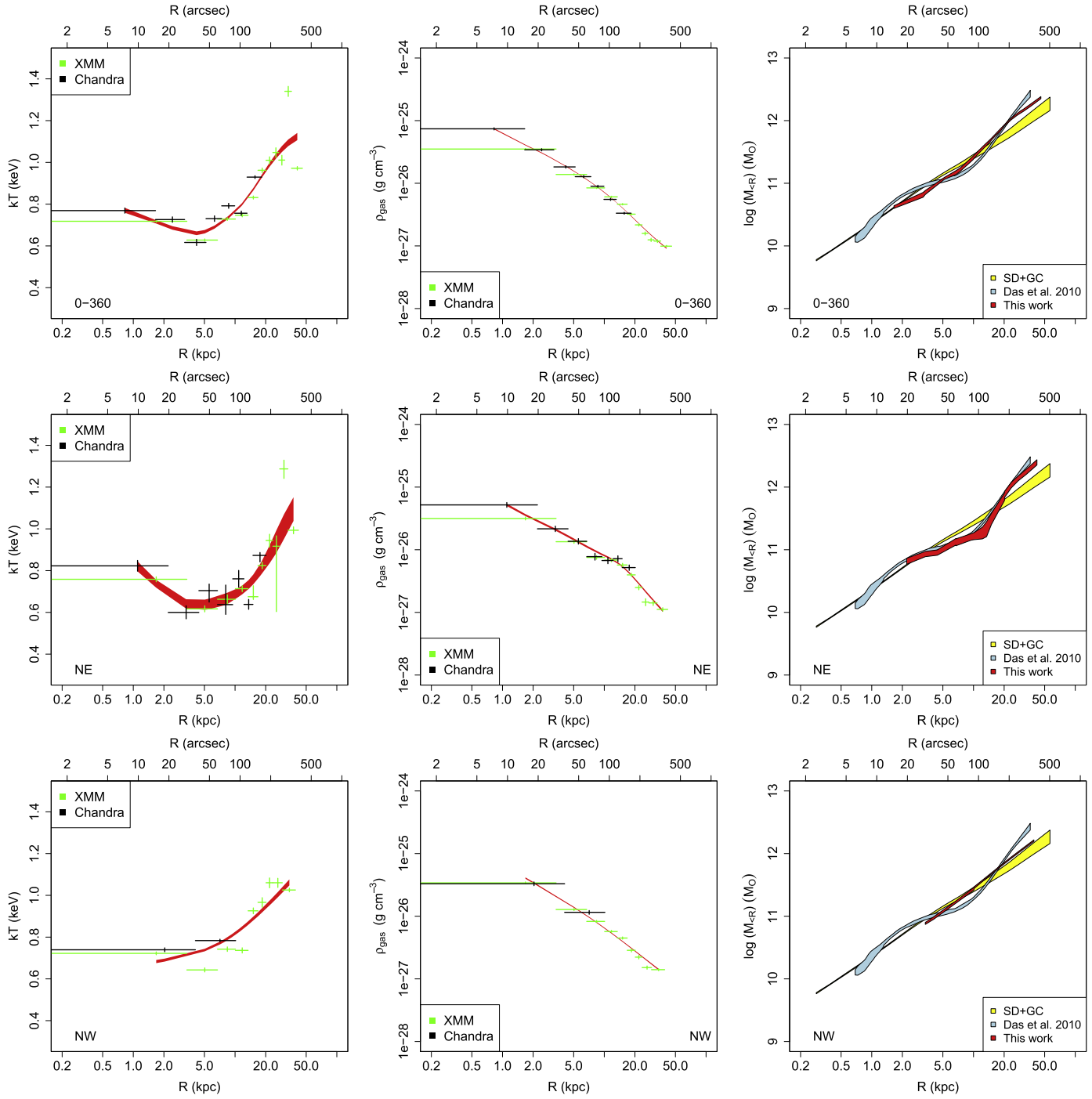

Figure 10. Gas profiles obtained in NGC 5846 with the reduction procedure proposed by Nevalainen et al. (2005). From top to bottom we show the profiles obtained in the full (0–360), NE (30–90), and NW (250–30) sectors, respectively. Spectra extracted in the annuli are then simultaneously fitted (separately for *XMM* and *Chandra* data) with the fixed abundance model and deprojected using the PROJCT model. The annuli width is chosen to reach a signal-to-noise ratio of 50, 30, and 50 for *XMM*-MOS data (represented in red) and of 100, 50, and 50 for *Chandra* ACIS data (represented in black) for the full (0–360), NE (30–90), and NW (250–30) sectors, respectively. Best fits of a smooth cubic spline are presented in red, with a smoothing parameter from top to bottom of 0.6, 0.6, and 0.7. In each row we show the gas temperature (first column) and density (second column) profiles. In the third column we present in red the total mass profiles obtained by means of Equation (1) from the best fits to gas temperature and density profiles. In the same panels we show in yellow the optical mass profile obtained from SD and GC reported by (Napolitano et al. 2014) and in light blue the X-ray mass profiles obtained by Das et al. (2010).

(2016) for both galaxies, Shen & Gebhardt (2010) for NGC 4649, and Napolitano et al. (2014) for NGC 5846). All mass values are corrected for the same distance as in Table 1.

For NGC 4649, the values of M_X extrapolated to $5R_e$ in the different sectors are consistent within the uncertainties, indicating that on 3–12 kpc scales the ISM distribution is relaxed and without strong anisotropies (see Figure 7). The effect of variable abundance is to yield flatter gas density and pressure profiles and then lower mass estimates. As expected, M_X obtained from the free abundance model is slightly lower than that from the fixed abundance model. However, within the measurement error, all models are generally consistent with the

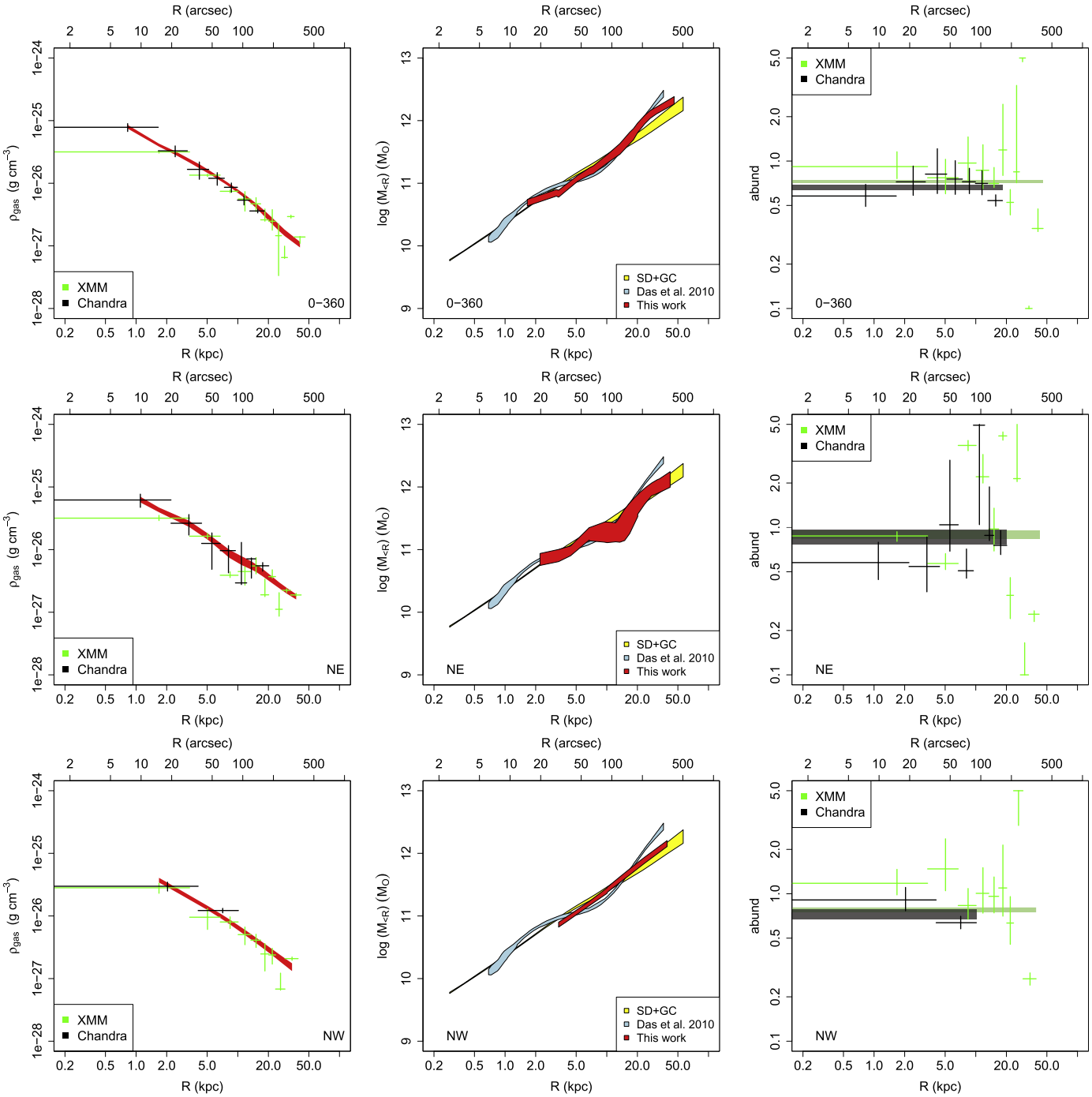

Figure 11. Same as Figure 10, but with the free abundance model (temperature profiles are similar to the fixed abundance model case and therefore omitted). In addition, in the rightmost panel of each row we show the element abundances profiles for *XMM*-MOS data (in green) and for *Chandra* ACIS data (in black). In the same panels we overplot with green and black rectangles the values of the element abundances obtained with the fixed abundance model for *XMM* and *Chandra* data, respectively.

previous X-ray (Humphrey et al. 2008) and kinematic (Alabi et al. 2016) mass measurements. The SE sector contains the diffuse tail reported by Woods et al. (2017), which appears faint when compared with simulations of gas stripping and Kelvin–Helmholtz instabilities in M89 (Roediger et al. 2015a, 2015b). According to these authors, the faintness of this structure could be due either to NGC 4649's larger distance from the cluster core (971 kpc) with respect to M89 (390 kpc) or to the fact that we may be observing this source shortly upon completing a turnaround in its orbit in Virgo. In any case the state of the gas in the tail is unclear, so we extended our analysis in the SE direction beyond 12 kpc. Table 4 includes the total mass value that we measure in this sector at $5R_e$ from X-ray data (without extrapolation). This value is indeed compatible with the extrapolated values obtained in this and other sectors, thus confirming that any deviation from HE in this region is small. The free abundance models are barely consistent with the Shen & Gebhardt (2010) optical model as

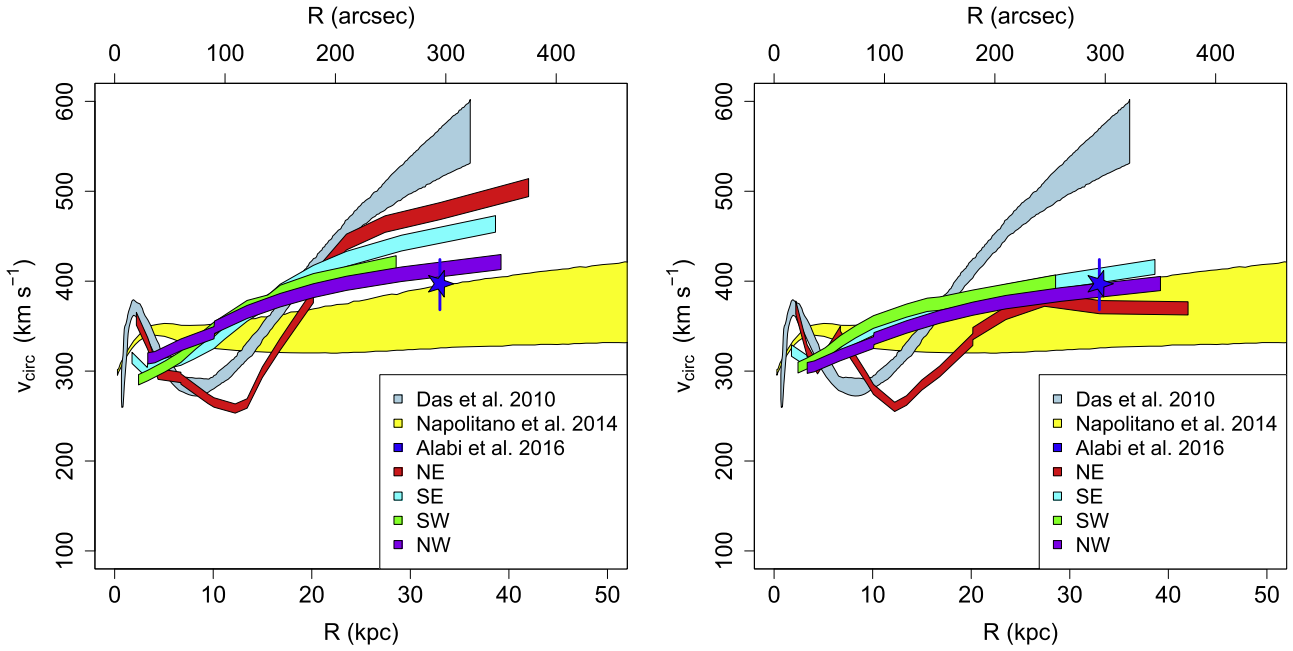

Figure 12. Left: comparison of velocity profiles of NGC 5846 from fixed abundance models. The profiles for different angular sectors are shown in different colors indicated in the legend, while the X-ray profile presented by Das et al. (2010) is shown in light blue, the SLUGGS SD+GC profile presented by Napolitano et al. (2014) is shown in yellow, and the blue star represents the measurement by Alabi et al. (2016), with the corresponding uncertainty shown with a vertical blue line. Right: same as the left panel, but for free abundance models.

noted by Pota et al. (2015, see their Section 8.3). More up-to-date data sets (Alabi et al. 2016) give a lower mass compatible with our X-ray HE mass profiles. Averaging the free abundance model extrapolated to $5R_e$, we can estimate $M_X(<5R_e) = (1.0 \pm 0.1) \times 10^{12}\,M_\odot$ for NGC 4649.

For NGC 5846, the highest value of M_X (in the NE sector for the fix abundance model) is compatible with the previous X-ray measurement by Das et al. (2010), but considerably higher (by 3σ) than the optical measurements by both Napolitano et al. (2014) and Alabi et al. (2016). As in NGC 4649, M_X obtained from the free abundance model is lower than that from the fixed abundance model. At the NW sector where the gas is most relaxed and extended, M_X is consistent with optical values. From this sector (using the free abundance model), we determine the total HE mass within five effective radii to be $M_X(<5R_e) = (1.2 \pm 0.2) \times 10^{12}\,M_\odot$ for NGC 5846. Since the X-ray data reach $R_{\rm max} \sim 6R_e$, we also evaluate $M_X(<6R_e) = (1.5 \pm 0.2) \times 10^{12}\,M_\odot$ for free abundance models.

4.4. Mass Decomposition

We tried decomposing the HE mass into various components and extrapolate the results to virial radius, to evaluate the contribution of the DM halo to the total mass. To do so, we fitted the observed mass profiles obtained in the different sectors with a model comprising the gas and stellar mass contribution, the central black hole, and DM. The gas mass profile is determined from the hot gas density profile. For the stellar mass profile, we use the ATLAS^{3D} r-band profiles presented by Scott et al. (2013) and assume a constant M_*/L_* ratio in a given galaxy. We note that, although some stellar light profiles from ATLAS^{3D} show some problems at radii larger than $\sim 250''$, these radii are in the region where DM is the dominant mass component, so they do not affect our results. Although different profiles have been proposed to describe the DM distribution in elliptical galaxies (e.g., Memola et al. 2011), here we assume the widely entertained Navarro, Frenk, and White (NFW; Navarro et al. 1997) profile $M_{DM}(<R) = 4\pi d_0 R_S^3 \left[\log\left(\frac{R_S+R}{R_S}\right) - \frac{R}{R_S+R}\right]$. We show the best-fit results of NGC 4649 and NGC 5846 in Figures 13 and 14, respectively. The gas, stars, BH, and DM are marked by a green dashed line, a blue dot-dashed line, a black dotted line, and a black dot-dashed line, respectively. We also show in both figures the optical mass profiles (in yellow) by Shen & Gebhardt (2010) and Napolitano et al. (2014) for NGC 4649 and NGC 5846, respectively, and $M_O(<5R_e)$ (blue star) from Alabi et al. (2016).

Since X-ray mass profiles assume HE, we expect this fitting procedure to yield results incompatible with similar estimates from optical derived profiles. In particular, for the mildly disturbed case of NGC 4649, we obtain $\langle M_{\rm BH}\rangle = (5.5 \pm 1.1) \times 10^9\,M_\odot$ and $\langle M_*/L_{*,r}\rangle = (4.4 \pm 0.4)\,M_\odot/L_\odot$ for fixed abundance models, while for free abundance models we get $\langle M_{\rm BH}\rangle = (5.1 \pm 0.9) \times 10^9\,M_\odot$ and $\langle M_*/L_{*,r}\rangle = (4.7 \pm 0.2)\,M_\odot/L_\odot$. The black hole mass so evaluated is compatible with the value of $M_{\rm BH} = (4.5 \pm 1.0) \times 10^9\,M_\odot$ reported by Shen & Gebhardt (2010), while our mass-to-light ratios $M_*/L_{*,r}$ are smaller than the value of 6.5 ± 0.4 (corrected for the distance used in this work) presented by Cappellari et al. (2013).

The discrepancies become more severe for the strongly disturbed case of NGC 5846, where we obtain $\langle M_{\rm BH}\rangle = (1.7 \pm 0.8) \times 10^{10}\,M_\odot$ and $\langle M_*/L_{*,r}\rangle = (2.8 \pm 0.6)\,M_\odot/L_\odot$ for fixed abundance models, while for free abundances we get $\langle M_{\rm BH}\rangle = (1.9 \pm 0.6) \times 10^{10}\,M_\odot$ and $\langle M_*/L_{*,r}\rangle = (2.3 \pm 0.5)\,M_\odot/L_\odot$. The black hole mass so evaluated is one order of magnitude larger than that reported by Graham (2008), $M_{\rm BH} = 1.1 \pm 0.2 \times 10^9\,M_\odot$, and estimated through velocity dispersion measurement, while our mass-to-light ratios are about one-third the value of 7.3 ± 0.5 presented by Cappellari et al. (2013) (again corrected for the distance used in this work),

Table 4
Results of the Mass Profile Fitting (with Uncertainties Reported in Parentheses)

(1) Source Name	(2) Sector	(3) $R_{\rm max}$ (kpc)	(4) $5R_{\rm e}$ (kpc)	(5) $M_X(<5R_e)$ ($10^{11}\,M_\odot$)	(6) $M_{X,\rm old}(<5R_e)$ ($10^{11}\,M_\odot$)	(7) $M_O(<5R_e)$ ($10^{11}\,M_\odot$)	(8) $M_O(<5R_e)$ ($10^{11}\,M_\odot$)	(9) $M_X(<6R_e)$ ($10^{11}\,M_\odot$)
NGC 4649	0–360 (FULL)	12.0*	25.1	12.4(0.3)*/11.2(1.7)*	11.2(0.9)	11.0(0.9)	16.2(5.7)	
	270–360 (NW)	11.4		12.1(0.5)*/8.5(1.7)*				
	0–90 (NE)	12.0*		12.0(0.4)*/10.9(2.6)*				
	90–180 (SE)	12.0* |25.5		12.0(0.5)*/12.3(3.6)* |12.4(0.9)/10.5(1.0)				
	180–270 (SW)	12.0*		10.8(0.5)*/9.8(1.5)*				
NGC 5846	0–360 (FULL)	45.9	33.0	16.0(0.6)/15.6(2.7)	22.2(2.2)	12.1(1.7)	10.1(1.9)	
	30–90 (NE)	42.0		18.1(2.0)/10.5(3.0)				
	90–180 (SE)	38.6		15.8(0.9)/12.9(1.9)				
	180–250 (SW)	28.6		13.9(0.7)*/12.8(1.6)*				
	250–30 (NW)	39.2		**13.1(0.3)/12.1(1.5)**				**16.4(0.5)/15.0(1.8)**

Note. (1) Name of the source. (2) Angular sector. (3) Maximum radius $R_{\rm max}$ reached in the present analysis. Values indicated with an asterisk are truncated to avoid disturbances in ISM due to the motion of NGC 4649 in the Virgo ICM as reported by Woods et al. (2017). In addition, for the SE direction of NGC 4649 we also report the value measured directly at $R_{\rm max}$ without truncation. (4) Five effective radii R_e as reported by Alabi et al. (2016). (5) Total mass enclosed in $5R_e$ calculated from the mass profile fits shown in Figures 13 and 14 (fixed/free abundance model). The values indicated with an asterisk are extrapolated to $5R_e$ from the fitting presented in Section 4.4. In addition, for the SE direction we also report the value of the total mass measured at $5R_e$. In boldface we indicate the value in the NW sector of NGC 5846 where $R_{\rm max} > 5R_e$ and we do not see strong deviations from HE. (6) Total mass enclosed in $5R_e$ extrapolated from previous X-ray profiles (Humphrey et al. (2008) for NGC 4649 and Das et al. (2010) for NGC 5846). (7) Total mass enclosed in $5R_e$ as reported by Alabi et al. (2016). (8) Total mass enclosed in $5R_e$ from previous optical profiles (Shen & Gebhardt (2010) for NGC 4649 and Napolitano et al. (2014) for NGC 5846). (9) Total mass enclosed in R_{6R_e} from the mass profiles presented in this work. Mass values are corrected for different distance adopted. In boldface we indicate the value in the NW sector of NGC 5846 where $R_{\rm max} > 6R_e$, and we do not see strong deviations from HE.

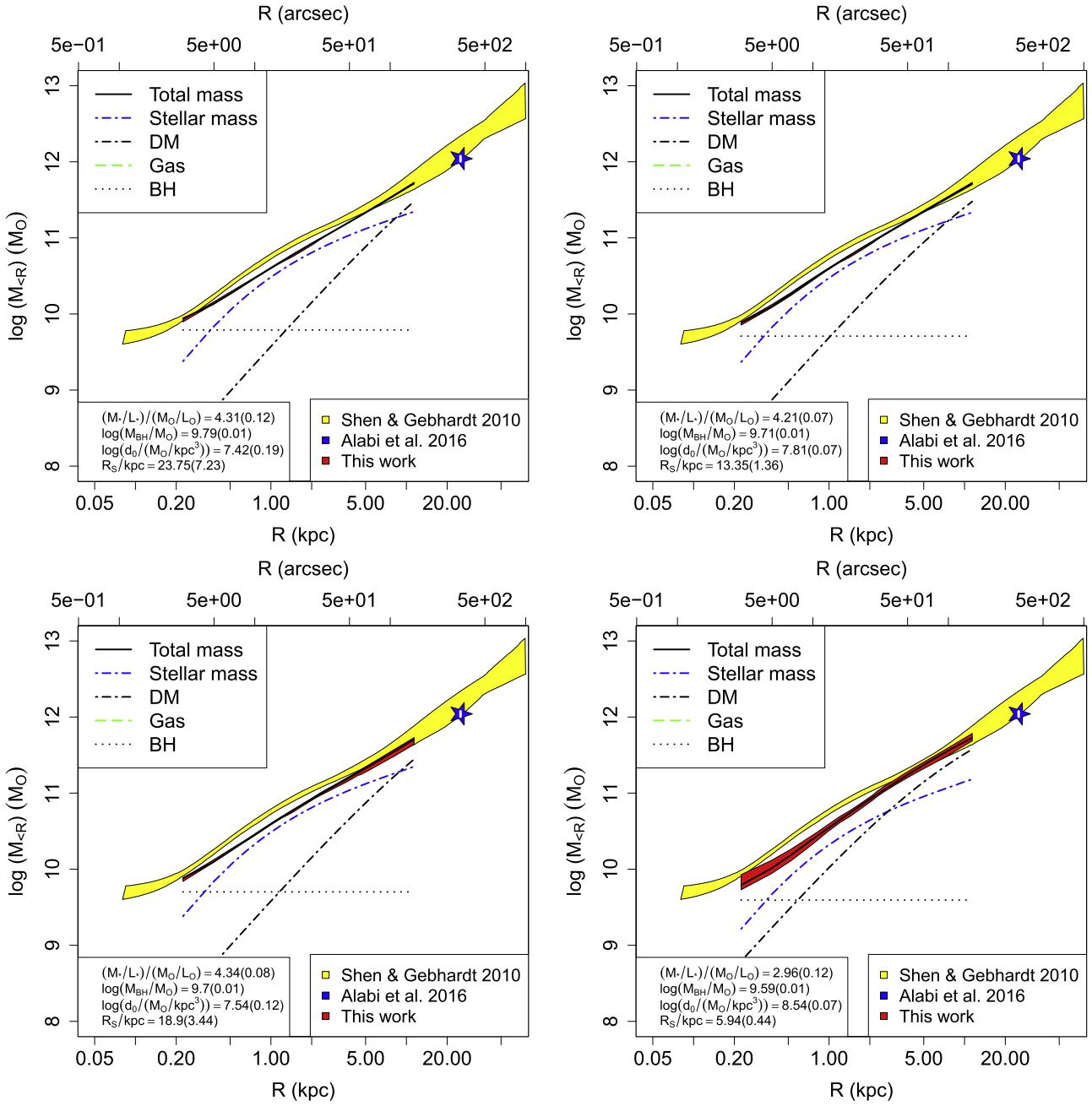

Figure 13. Fit to mass profiles of NGC 4649 obtained with fixed (top row) and variable (bottom row) element abundances, in the full (0–360; left panels) and SW (180–270; right panels) sectors. The mass profile from the HE equation is presented in red, and the best-fit contributions of the various mass components (gas mass, stellar mass, black hole, and NFW DM profile) are presented with different colors as reported in the legend. The best-fit parameters are reported in the lower left box. In yellow we show the optical mass profile obtained from SD and GC reported by Shen & Gebhardt (2010), while the blue star represents the measurement by Alabi et al. (2016), with the corresponding uncertainty shown as a white vertical line inside the star itself.

although consistent with the range of mass-to-light ratios found for ellipticals in these authors' study.

We then tried fixing the $M_*/L_{*,r}$ and $M_{\rm BH}$ to their literature values and evaluating the DM component as the difference between the total X-ray mass profile and the stellar, black hole, and gas mass components. As mentioned before, the values of $M_*/L_{*,r}$ obtained from optical data are higher than those we obtain from X-ray data, due to the previously discussed deviations from HE that may affect this technique, and this difference is more severe in the case of NGC 5846, where the ISM is more disturbed. As a consequence, the DM profile can appear to be negative at small radii, where the ISM is away from HE, and it can be considered reliable only at large radii (where the total X-ray and optical mass profiles are compatible).

This analysis shows that mass measurement and characterization only based on X-ray data can lead to misleading results, due to the very nature of the ISM physics resulting in the X-ray emission, and it requires a selection of azimuthal directions in which the ISM can be considered fairly relaxed as a consequence of comparisons with optical profiles. Other assumptions—like abundance or DM profiles—make the extrapolation of these results to radii much larger than those attained by X-ray analysis and up to the virial radius even more problematic.

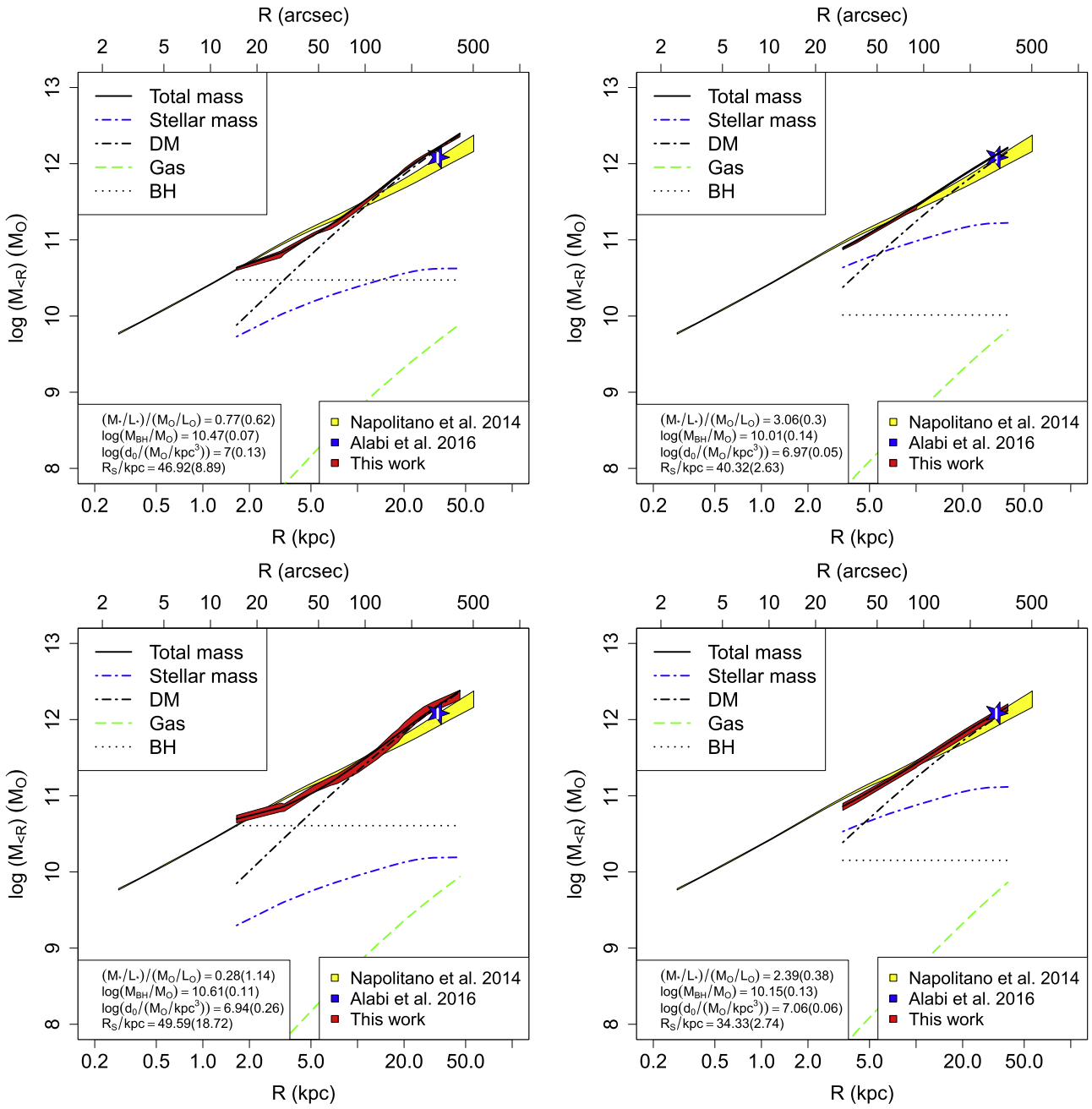

Figure 14. Fit to mass profiles of NGC 5846 obtained with fixed (top row) and variable (bottom row) element abundances, in the full (0–360; left panels) and NW (250–30; right panels) sectors. The mass profile from the HE equation is presented in red, and the best-fit contributions of the various mass components (gas mass, stellar mass, black hole, and NFW DM profile) are presented with different colors as reported in the legend. The best-fit parameters are reported in the lower left box. In yellow we show the optical mass profile obtained from SD and GC reported by Napolitano et al. (2014), while the blue star represents the measurement by Alabi et al. (2016), with the corresponding uncertainty shown as a white vertical line inside the star itself.

5. Summary and Conclusions

We present the results of a joint *Chandra XMM-Newton* analysis of two ETGs. NGC 4649 shows a relaxed and symmetric X-ray morphology in the range 3–12 kpc, while on larger scales there are evidences of gas stripping due to the galaxy motion in the cluster ICM. NGC 5846, on the other hand, shows signatures of mild sloshing at all radii. We make use of X-ray-based mass profiles in various azimuthal directions to investigate these effects on the ISM by comparison with optically based mass profiles and studied the effects of different background subtraction/modeling procedures and element abundance gradients on the total mass evaluation. The main results of this analysis are as follows:

1. The X-ray mass profiles of NGC 4649 appear to be fairly smooth in the range 3–12 kpc and do not show azimuthal asymmetries. The values of M_X extrapolated to $5R_e$ in different directions are consistent with each other and with M_X measured at $5R_e$ in the SE sector that contains the faint tail structure.
2. In NGC 5846 the X-ray-derived mass profiles show significant asymmetries in the ISM distribution, especially in the NE direction, where the halo shows evidence of interaction with the group companion spiral galaxy NGC 5850. The comparison with optical mass profiles shows in this direction evidence of gas compression and

decompression due to gas sloshing on scales larger and smaller than ∼15 kpc, respectively, and these effects disappear in the NW direction where the emission is smooth and extended.
3. Deviations between the optical and X-ray profiles for $r < 10$ kpc are observed in all sectors of NGC 5846, and they are interpreted as the consequence of ISM disturbances connected with recent AGN activity. On larger scales, instead, the match between X-ray (from the NW sector) and optical data is recovered after allowing for element abundance gradients, which shows decreasing abundances in the outer regions of the galaxy.
4. Mass measurement solely based on X-ray data can lead to misleading results if not coupled with the selection of azimuthal sectors in which the ISM can be considered fairly relaxed. Using the sectors with relaxed gas distribution, we measured the total mass (based on X-ray data) of $(1.2 \pm 0.2) \times 10^{12}\,M_{\odot}$ for NGC 5846 at five effective radii, while an extrapolation to $5R_e$ of the profile of NGC 4649 yields $(1.0 \pm 0.1) \times 10^{12}\,M_{\odot}$. These values are consistent with those from previous optical measurements (Das et al. 2011; Napolitano et al. 2014; Alabi et al. 2016).
5. Using the NW sector of NGC 5846, for which there is good agreement with optical mass profiles, we measure a mass at $6R_e$ of $M_X(<6R_e) = (1.5 \pm 0.2) \times 10^{12}\,M_{\odot}$.
6. We also performed fits of the mass profiles to evaluate the contributions of BH, gas, stars, and DM to the total mass. While the DM dominates at large radii, as expected, the measurements of the BH mass are complicated by the difficulty in disentangling it from the stellar mass contribution. In addition, the X-ray-derived mass profiles rely on the HE assumption, which as shown here, cannot be the case, due to either nuclear activity or galactic interactions. Therefore, virial mass evaluation is subject to significant uncertainties due to uncertain extrapolation of the observed gas profiles to the virial radius, which usually lies far beyond the maximum extent attained by the X-ray detectors.

This work was supported by the *Chandra* grant AR5-16007X and by 2014 Smithsonian Competitive Grant Program for Science. G.F. thanks the Aspen Center for Physics, funded by NSF grant no. 1066293, for their hospitality while this paper was completed. A.J.R. was supported as a Research Corporation for Science Advancement Cottrell Scholar. This work was also supported by NSF grants AST-1211995, AST-1616598, and AST-1616710.

Appendix A
Background Subtraction

In this section we present the details of the different reduction procedures tested in this work for the *XMM-Newton* MOS data. In particular, our main aim here is to compare the impact of different ways of evaluating the background (both astronomical and instrumental) for these data.

A.1. Simple Background Subtraction

Following Nevalainen et al. (2005), we filtered MOS1 and MOS2 data for hard-band flares by excluding the time intervals where the 9.5–12 keV count rate evaluated on the whole detector FOV was more than 3σ away from its average value. To achieve a tighter filtering of background flares, we iteratively repeated this process two more times, re-evaluating the average hard-band count rate and excluding time intervals more than 3σ away from this value. The same procedure was applied to the soft 1–5 keV band, restricting the analysis to an annulus with inner and outer radii of $12'$ and $14'$, where the emission from the galaxy is expected to be small.

The background was evaluated from appropriate blank-sky files (Carter & Read 2007) filtered in the same way as the event files. Following Nevalainen et al. (2005), we normalized the blank-sky file exposures to match the 9.5–12 keV count rate of the event files, since at these energies we expect to see only the particle background. However, since the particle background and the sky background are independent, we apply this normalization only in the 2–7 keV band (where the sky background contribution is expected to be only ∼20%) and not to the 0.5–2 keV band (where the sky background is expected to dominate). We then excluded from the spectral fitting (see Section 3.3) the 1.45–1.55 keV band, due to variable Al K lines.

A.2. Double Background Subtraction

The second reduction method is that proposed by Arnaud et al. (2001, 2002). The GTI filtering is performed on the whole detector FOV excluding time intervals where the 10–12 keV count rate was larger than 0.15 counts s^{-1}. We made use of the blank-sky files, again filtered in the same way as the event files, and with exposure normalized to match the 10–12 keV count rate of the event files.

To disentangle the cosmic X-ray background from the instrumental background, we made use of vignetting-corrected event files (produced with the EVIGWEIGHT SAS task), since the cosmic X-ray background can be considered uniform on scales $\sim 30'$ but is affected by vignetting, while the instrumental background is nonuniform but is not vignetted. Following Arnaud et al.'s "double subtraction" procedure, we first subtracted from the source spectrum (extracted for a region of area A) the spectrum extracted in the same region from the blank-sky file, obtaining the net spectrum I. Then we performed the same procedure, but from a region (of area A') of the FOV that we *assumed* to be source free, obtaining the net spectrum I'. Finally, we subtracted these two net spectra taking into account the ratio of the extraction region areas. The resulting spectrum $S = I - I'(A/A')$ is expected to contain only source emission.

A.3. Background Modeling

The third reduction method we adopted is the one proposed in the "Cookbook for Analysis Procedures for *XMM-Newton* EPIC Observations of Extended Object and the Diffuse Background"[14] (Snowden & Kuntz 2011). The GTI filtering for this procedure is preformed extracting 8–12 keV light curves both in annulus away from the central source in the exposed FOV and in the unexposed detector corners, and then excluding the time intervals for which the former count rate exceeds 1.2 times the latter count rate.

The background for this reduction method is partly subtracted and partly modeled. In particular, QPB spectra are created through the MOS_BACK task and subtracted from the source spectra. In addition, we modeled the instrumental and the cosmic background as follows. We modeled the Al

[14] https://heasarc.gsfc.nasa.gov/docs/xmm/esas/cookbook/xmm-esas.html

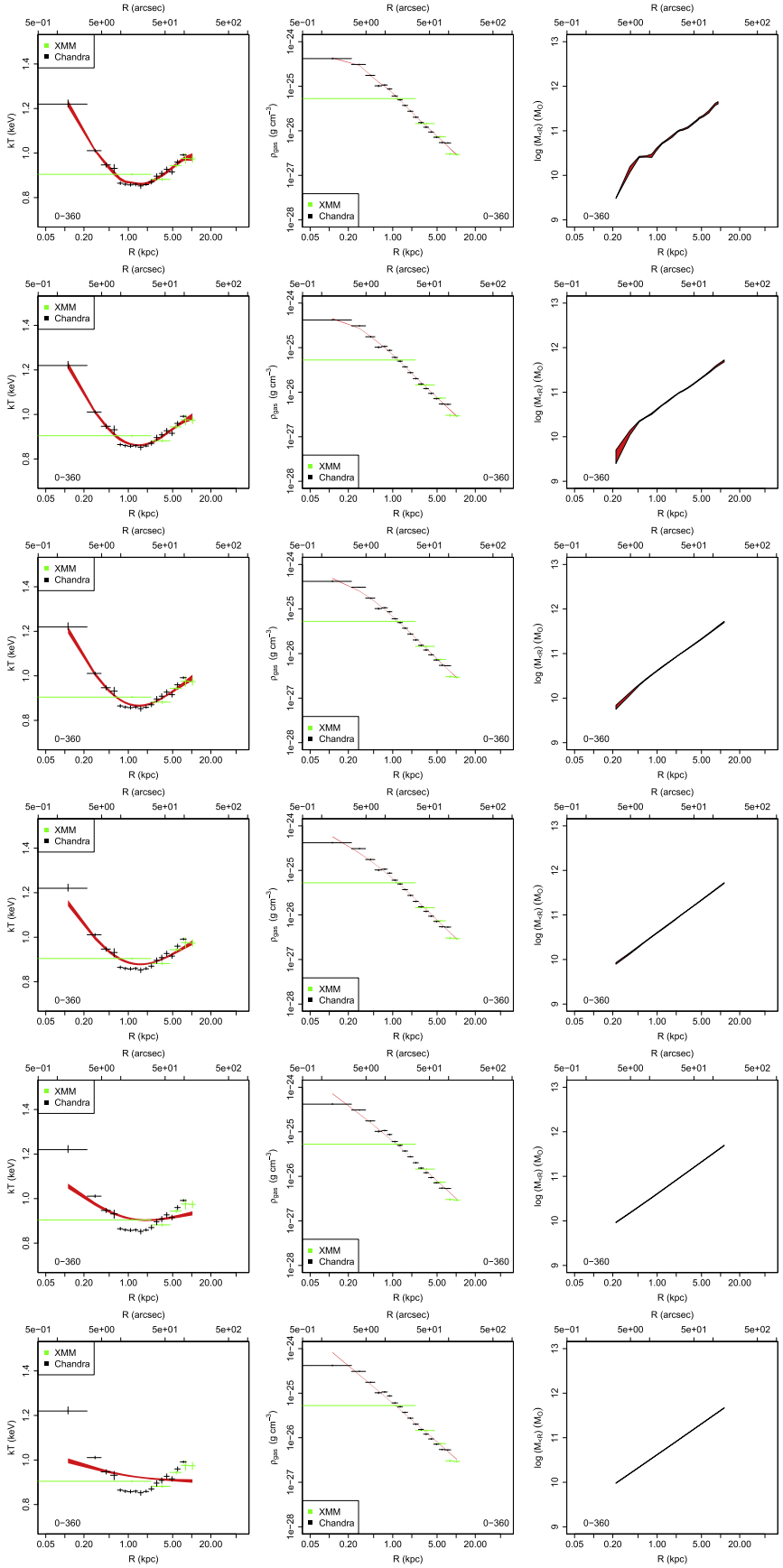

Figure 15. Effect on the X-ray mass profiles of the increasing smoothing parameter of the spline model used for fitting the gas profiles. From left to right we present the gas temperature, gas density, and resulting mass profile for the full (0–360) sector of NGC 4649 for a minimum signal-to-noise ratio of 50 for *XMM-Newton* and 100 for *Chandra* data, respectively. From top to bottom we show increasing smoothing parameters from 0.5 to 1 with a 0.1 increase.

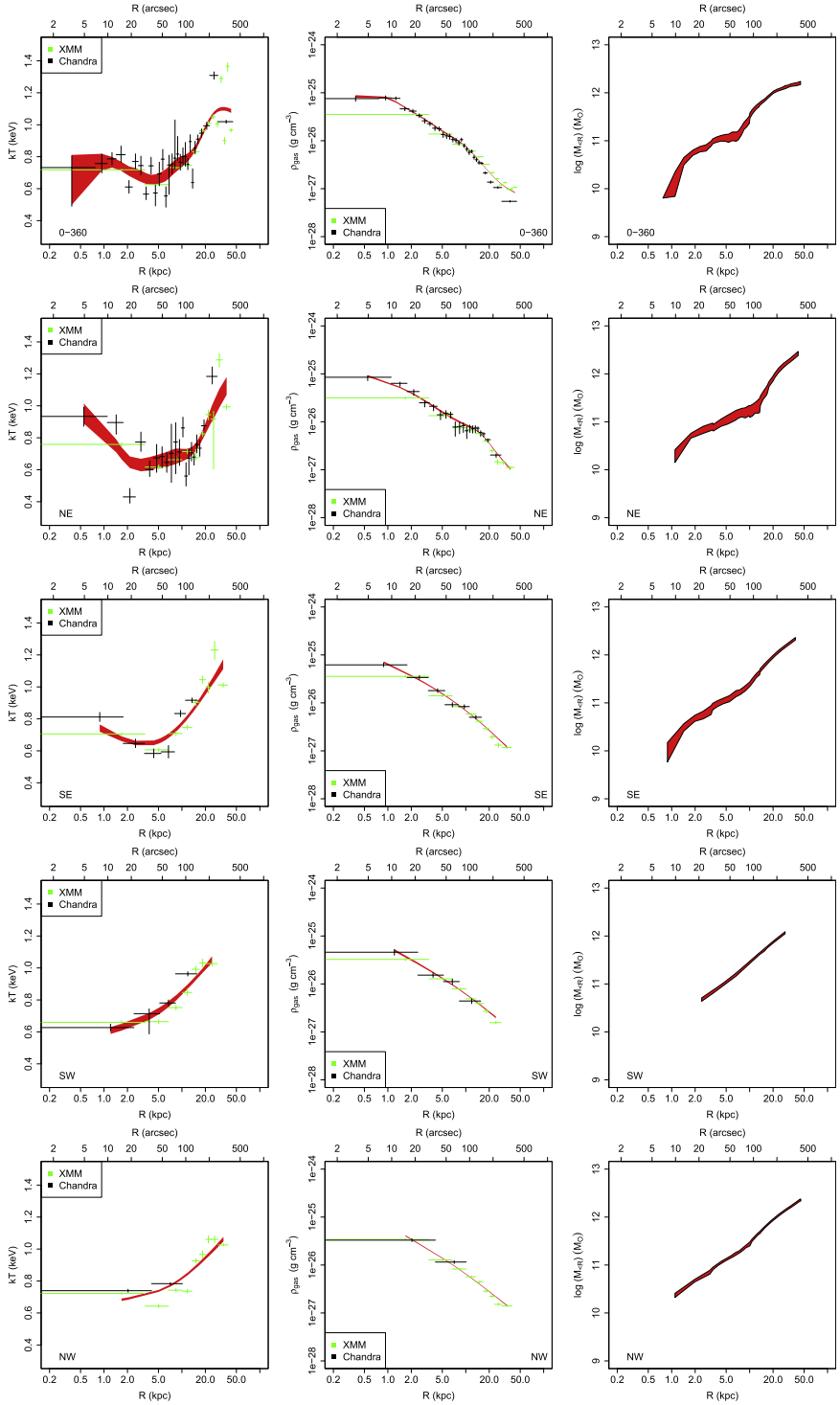

Figure 16. Effect on the X-ray mass profiles of the different sectors selected for the spectral extraction. From left to right we present the gas temperature, gas density, and resulting mass profile for NGC 5846 (with a smoothing parameter of 0.7), while from top to bottom we show the results in the full (0–360), NE (30–90), SE (90–180), SW (180–250), and NW (250–30) sectors, respectively. The minimum signal-to-noise ratio is 30 for *XMM-Newton* data in all sectors, while for *Chandra* data the minimum signal-to-noise ratio is 50 in the full (0–360), SW (180–250), and NW (250–30) sectors and 30 in the NE (30–90) and SE (90–180) sectors.

Kα and Si Kα lines with Gaussian lines at $\sim$1.49 and $\sim$1.75 keV, and the soft proton component as a power law that is not folded through the instrumental effective area (adding in XSPEC a separate model with a diagonal unitary matrix). As for the cosmic background, we modeled the local hot bubble with a cool ($\sim$0.1 keV) unabsorbed thermal component, the cooler halo with a $\sim$0.1 keV absorbed thermal component, and the hotter halo and/or intergalactic medium with a higher temperature $\sim$0.25–0.7 keV absorbed thermal component.

As mentioned in the main text, this method requires a complex spectral modeling, with several free parameters that make it

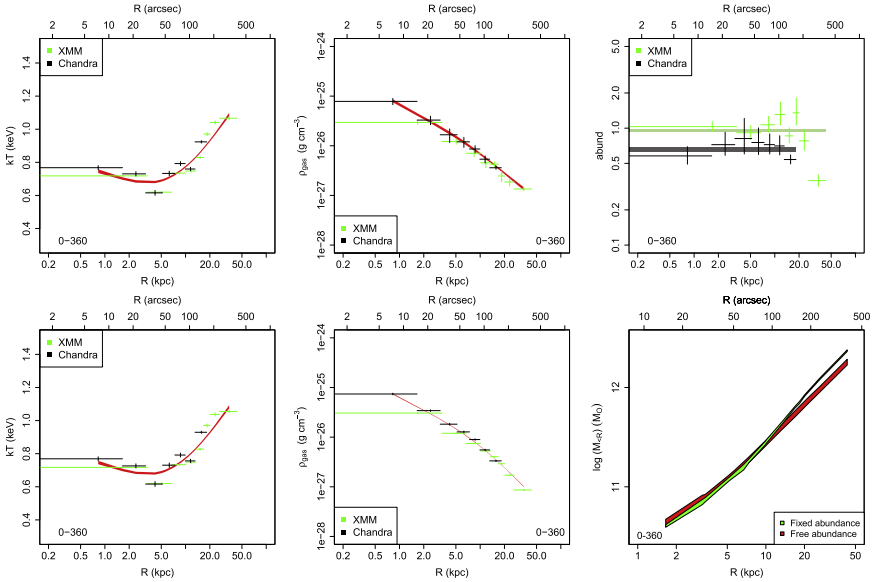

Figure 17. Effect on the X-ray mass profiles of the free element abundance. In the top panels we present results from the free abundance model for NGC 5846 in the full (0–360) sector; in particular, from left to right we show the gas temperature, gas density (with the best-fit spline model with a smoothing parameter of 0.7 overplotted), and abundance profiles. In the bottom panels we present results from the fixed abundance model; from left to right we show the gas temperature profile, the gas density profile, and a comparison between the mass profiles obtained from the fixed (green) and free (red) abundance models. The minimum signal-to-noise ratio is 100 for both *XMM-Newton* and *Chandra* data.

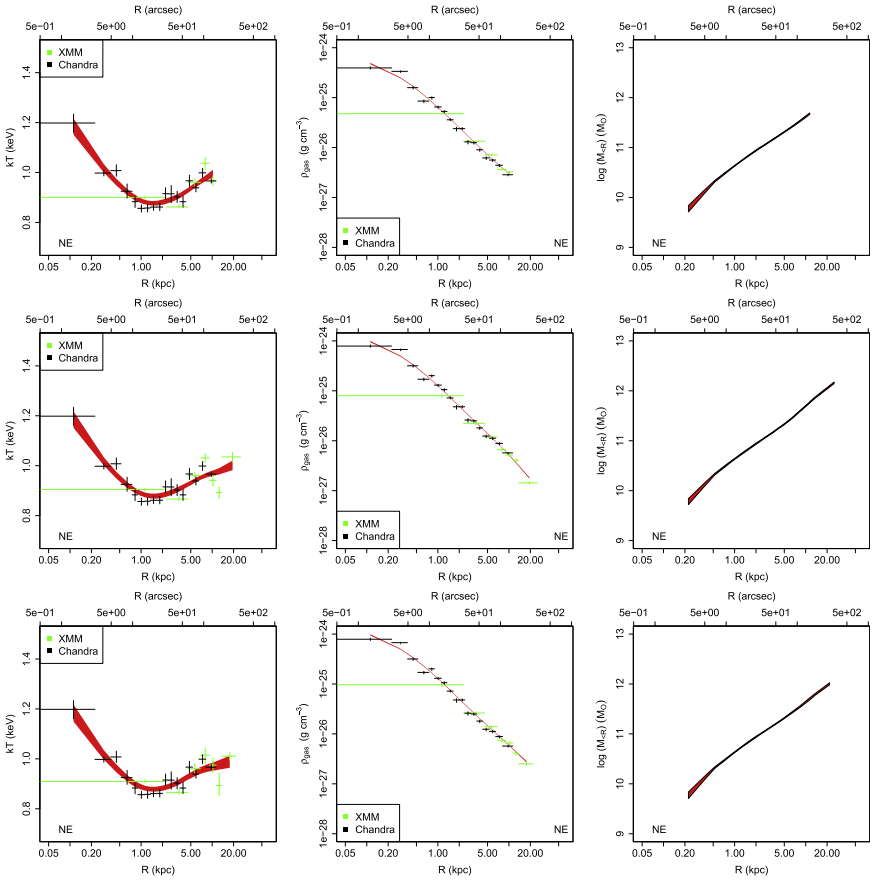

Figure 18. Effect of the different background subtraction procedures on the X-ray gas profiles of NGC 4649 in the NE (0–90) sector. From left to right we show the gas temperature, gas density (with the best-fit spline model with a smoothing parameter of 0.7 overplotted), and resulting mass profile for Nevalainen et al., Arnaud et al., and Snowden & Kuntz in the top, middle, and bottom rows, respectively. The minimum signal-to-noise ratio is 30 and 50 for *XMM-Newton* and *Chandra* data, respectively.

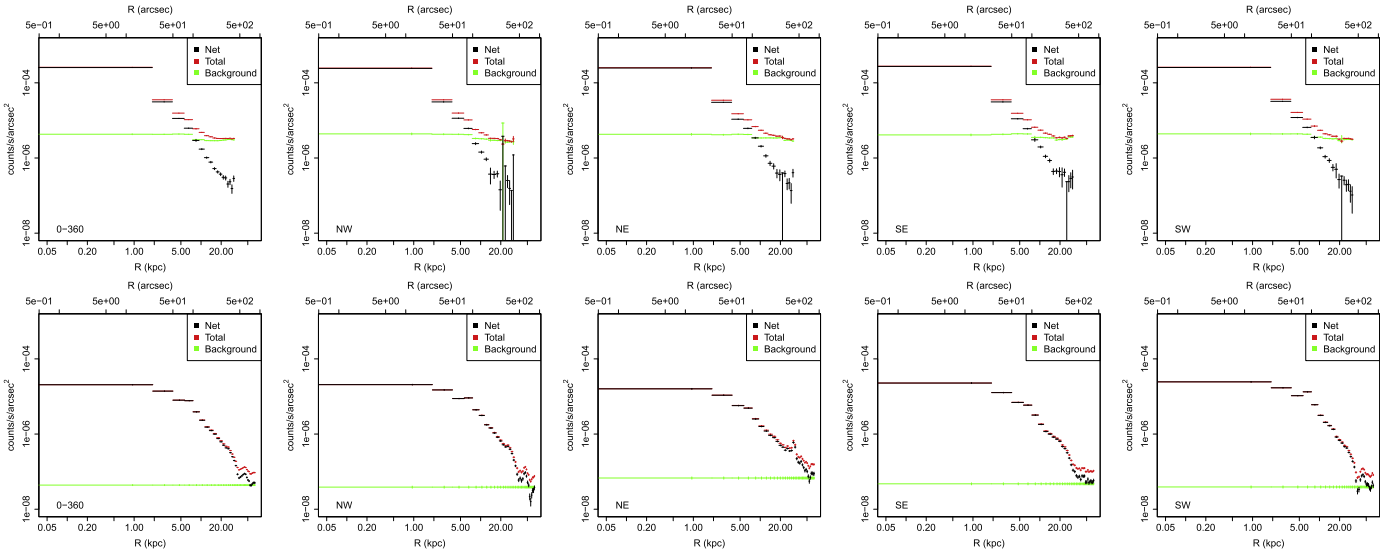

Figure 19. Brightness profiles for NGC 4649 in the 0.3–10 keV band in the different sectors shown in Figure 1, for (from left to right) full (0–360), NW (270–360), NE (0–90), SE (90–180), and SW (180–270), respectively. In particular, we show brightness profiles for *Chandra* ACIS data in the top row and for the *XMM*-MOS data obtained from the reduction procedure proposed by Nevalainen et al. (2005) in the bottom row. The annuli width is ∼25″, 50 pixels for *Chandra* ACIS data and 500 pixels for *XMM*-MOS data. Red, black, and green points represent total, net, and background brightness profiles, respectively.

difficult to find stable fitting convergence in unsupervised analysis procedures (especially in conjunction with 3D deprojection; see Section 3.3). To avoid this problem, in the spectral fitting procedure we used as starting values of the gas component (see Section 3.3) the best-fit value obtained with the procedure discussed in Appendix A.1.

Appendix B
Model Effects

Here we show in detail the effects that the various parameters in our modelization can have on the final mass profile, namely, the smoothing parameter of the spline function used to fit the gas profiles (B.1), the different angular section used for the spectral extraction (B.2), the element abundances (B.3), and the different background subtraction (B.4).

B.1. Effects of the Spline Function Smoothing

As shown in Figure 15, lower values of the smoothing parameter yield best-fit models that are able to represent all the finer details of the gas profiles, while higher values of the smoothing parameter favor monotonic profiles. In the same figure we show the effects of the increasing smoothing parameter on the mass profile resulting from Equation (1). The choice of the smoothing parameter value is a trade-off between the best-fit function ability to represent the finer details of the gas profiles and the need to get rid of the noise in these profiles in order to get meaningful physical results, that is, a combination of temperatures and slopes that yields decreasing or even negative values in the mass profiles. On the other hand, however, these apparently unphysical results may be the consequence of gas conditions away from HE. In the case presented in Figure 15, for example—that is, gas profiles for NGC 4649 in the full (0–360) sector for the Nevalainen et al. reduction procedure—a value of the smoothing parameter of 0.5 yields noisy mass profiles, particularly steep in the inner bins. On the other hand, for values of the smoothing parameter larger than or equal to 0.8 the mass profile is very smooth, but the best-fit models deviate significantly from the data. In this case, therefore, the optimal choice for the smoothing parameter is 0.7. The smoothing parameters chosen in the other cases are reported in the captions of Figures 7 and 10.

B.2. Effects of the Sector Direction

We note that the total mass obtained from Equation (1) is the total mass enclosed within a radius R assuming spherical symmetry, that is, the total mass assuming that the gas is in HE and distributed in a spherical shell with constant temperature. Therefore, even if we extract spectra in angular sectors, it will make sense to compare the resulting mass profiles with each other and with the mass profiles from optical markers.

In Figure 16 we show how the X-ray-derived mass profiles depend on the sector chosen for the spectral extraction in the source NGC 5846 (with a smoothing parameter of 0.7). As recalled in Section 2, this source shows evidence of gas sloshing as a consequence of the interaction with the group companion NGC 5850 in the NE (30–90) direction, reflecting in a disturbed X-ray morphology. As a matter of fact, the full (0–360) mass profile shows a break between 1 and 2 kpc followed by a sudden increase at ∼10 kpc. When we isolate the mass profiles extracted in different directions, we can see that these effects are mainly driven by the gas in the NE sector—that is, in the NE direction—while these effects weaken in other sectors where the profiles are smoother and without indication of strong disturbances in the ISM.

B.3. Effects of the Variable Element Abundances

In Figure 17 we show the effects of metal abundances on the best-fit model to the gas profiles (and the resulting mass profiles) for the NW (250–30) sector of NGC 5846 (both with smoothing parameter of 0.7). In particular, in the left and

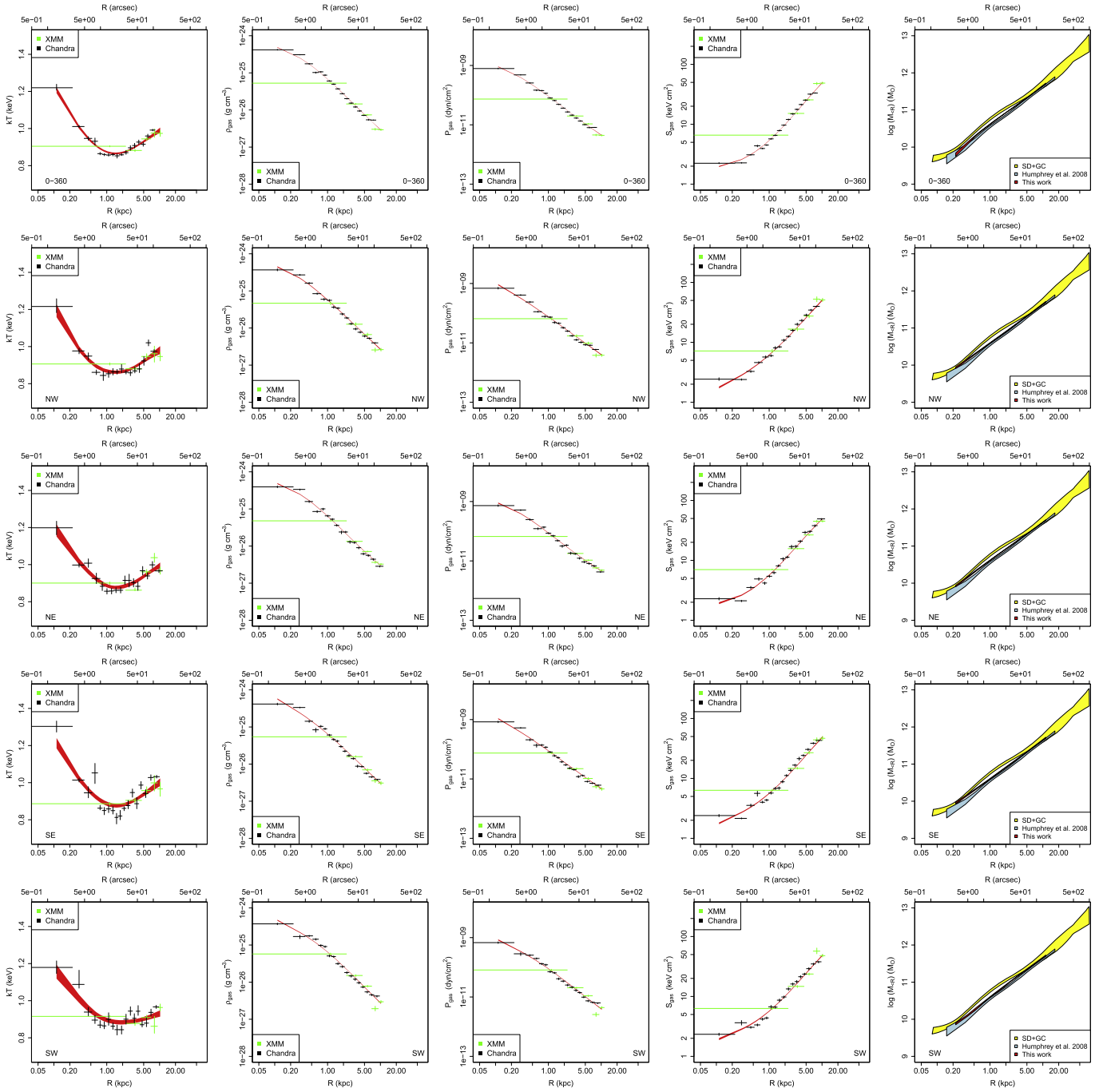

Figure 20. Gas profiles obtained in NGC 4649 with the reduction procedure proposed by Nevalainen et al. (2005). From top to bottom we show the profiles obtained in the full (0–360), NW (270–360), NE (0–90), SE (90–180), and SW (180–270) sectors, respectively. In each row we show from left to right the gas temperature, density, pressure, and entropy, respectively. Spectra extracted in the annuli are then simultaneously fitted (separately for *XMM* and *Chandra* data) with the fixed abundance model and deprojected using the PROJCT model. The annuli width is chosen to reach a signal-to-noise ratio of 30 for *XMM*-MOS data (represented in red) and of 50 for *Chandra* ACIS data (represented in black), with the exception of the full (0–360) sector, for which we chose a signal-to-noise ratio of 50 for *XMM* data and 100 for *Chandra* data. Best fits of a smooth cubic spline are presented in red, with smoothing parameter from top to bottom of 0.8, 0.8, 0.7, 0.8, and 0.8. In the rightmost panels we present in red the total mass profiles obtained by means of Equation (1) from the best fits to gas temperature and density profiles. In the same panels we show in yellow the optical mass profile obtained from SD and GC reported by Shen & Gebhardt (2010) and in light blue the X-ray mass profiles obtained by Humphrey et al. (2008).

middle panels of the top and bottom row we show the gas temperature and density profiles resulting from the free and fixed abundance models, respectively. In addition, in the right panel of the top row we show the abundance profiles compared with the averaged values of the abundances obtained with the fixed abundance model. Although the abundance profile is rather noisy, we see that it tends to decrease at larger radii, and this yields flatter gas density profiles and therefore smaller enclosed mass as estimated from Equation (1), as shown in the right panel of the bottom

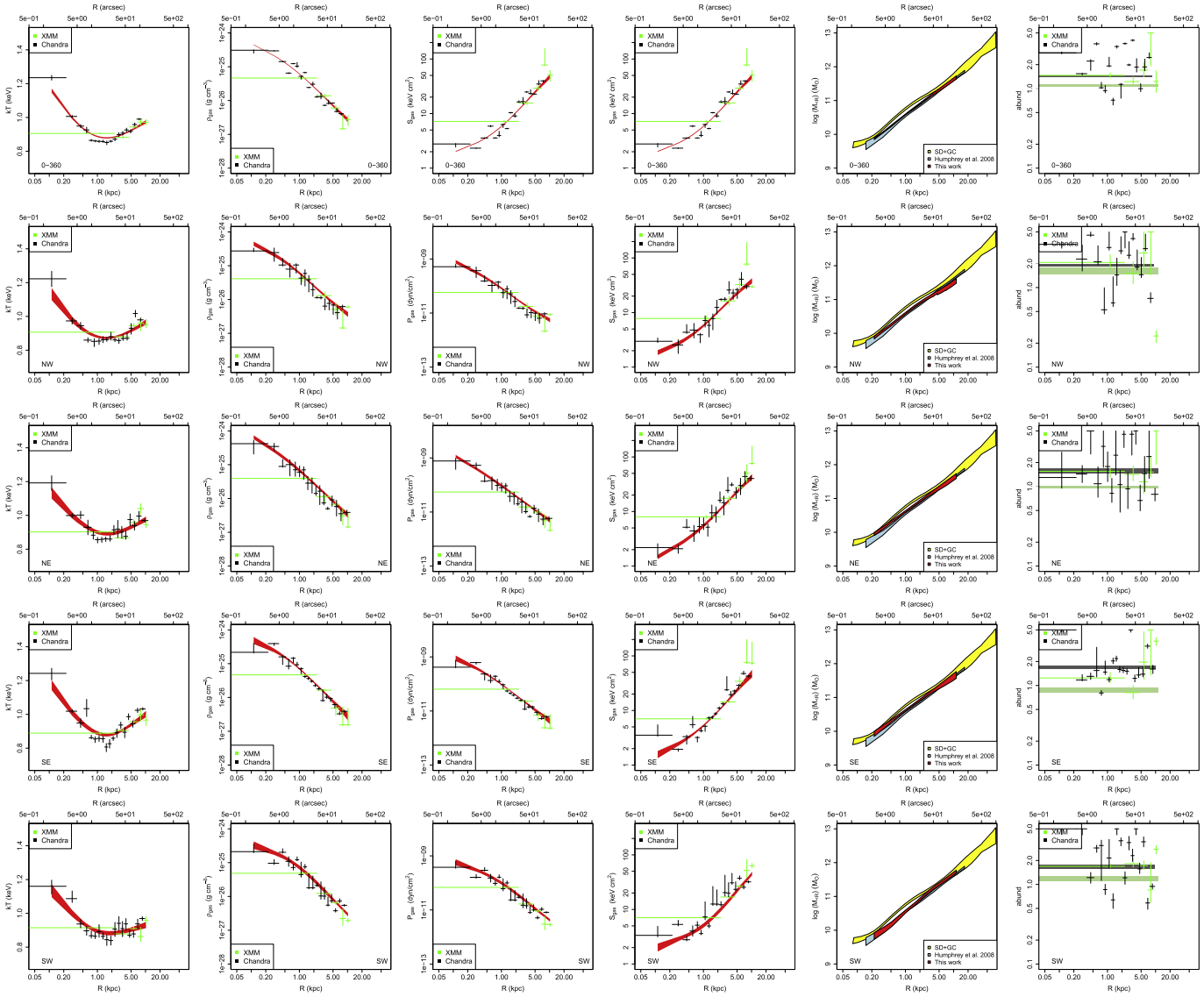

Figure 21. Same as Figure 20, but with the free abundance model. In addition, in the rightmost panel of each row we show the element abundances profiles for *XMM*-MOS data (in green) and for *Chandra* ACIS data (in black). In the same panels we overplot with green and black rectangles the values of the element abundances obtained with the fixed abundance model for *XMM* and *Chandra* data, respectively.

row of the same figure. In addition, allowing variable abundances yields in general larger uncertainties (especially on gas density), which in turn translates to larger uncertainties on the enclosed mass profile.

B.4. Effects of the Background Subtraction Method

In Figure 18 we show the effects of the different background subtractions on the gas and mass profiles of NGC 4649 in the NE (0–90) direction (all the profiles have a smoothing parameter of 0.7). As evident, the different background subtraction methods yield similar gas and mass profiles, with only minor effects on the outer bins at fainter surface brightnesses. For the double subtraction method we have to assume a source-free region that will be excluded by our spectral extraction. In particular, we selected a sector between 13′ and 14′ in the SE direction for both NGC 4649 and NGC 5846, so the main effect of the background subtraction proposed by Arnaud et al. (2001, 2002) is to restrict our analysis to smaller radii in this sector with respect to the other methods.

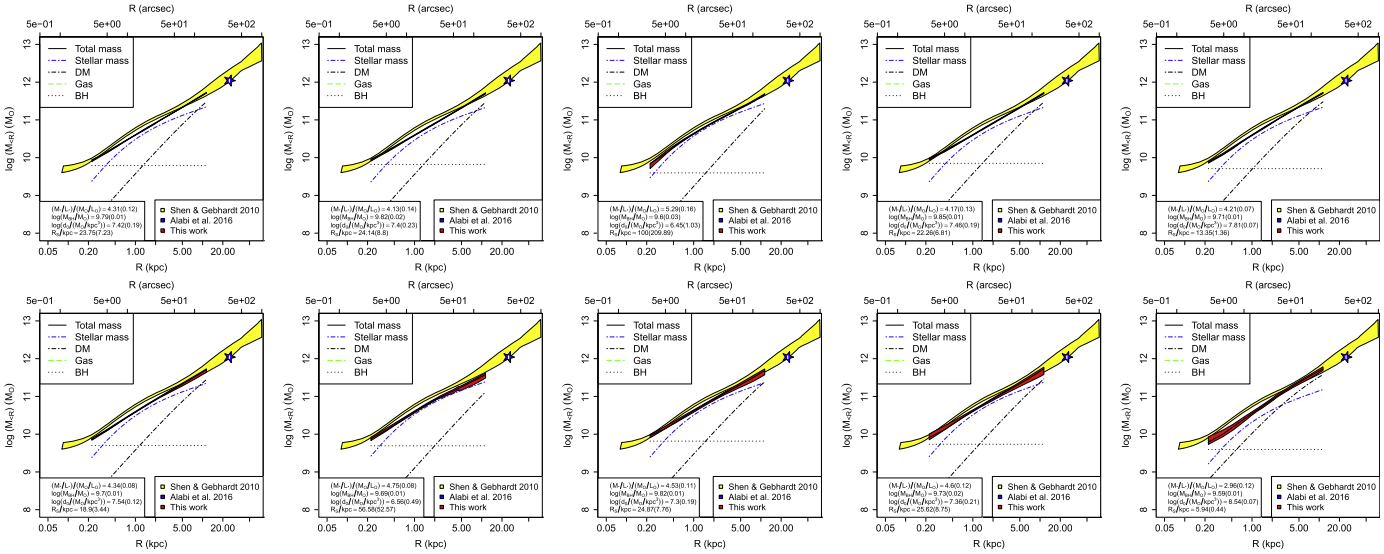

Figure 22. Fit to mass profiles of NGC 4649 shown in Figure 20 (top row) and in Figure 21 (bottom row), from left to right in the full (0–360), NW (270–360), NE (0–90), SE (90–180), and SW (180–270) sectors, respectively. The mass profile from the HE equation is presented in red, and the best-fit contributions of the various mass components (gas mass, stellar mass, black hole, and NFW DM profile) are presented with different colors as reported in the legend. The best-fit parameters are reported in the lower left box. In yellow we show the optical mass profile obtained from SD and GC reported by Shen & Gebhardt (2010), while the blue star represents the measurement by Alabi et al. (2016), with the corresponding uncertainty shown as a white vertical line inside the star itself.

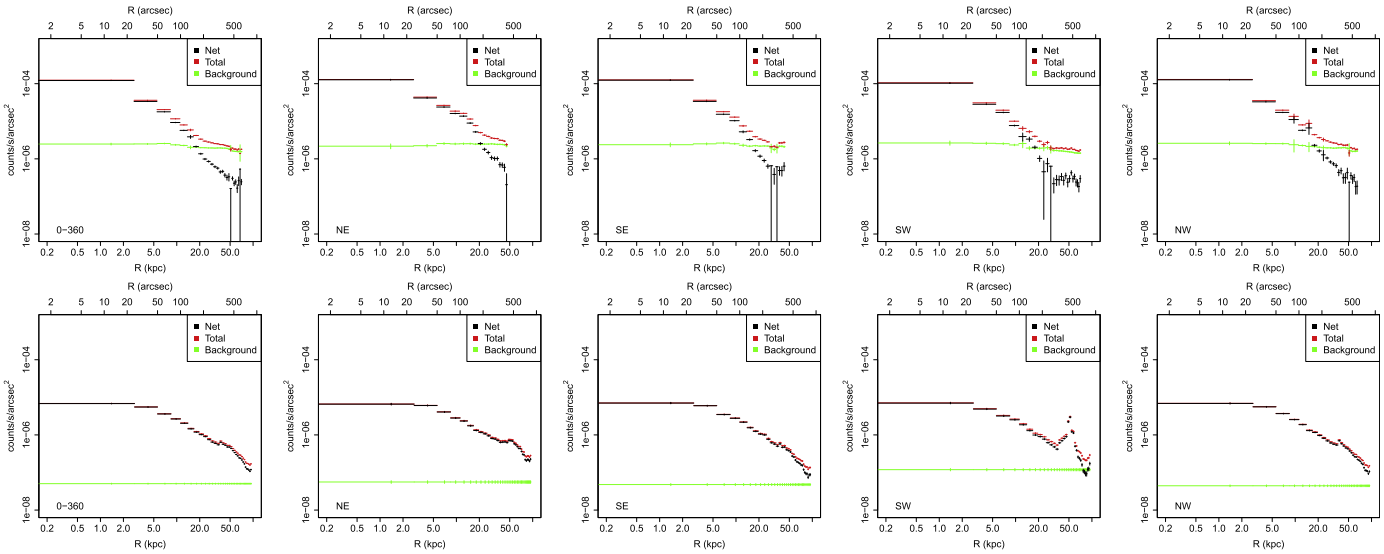

Figure 23. Brightness profiles for NGC 5846 in the 0.3–10 keV band in the different sectors shown in Figure 4, for (from left to right) full (0–360), NE (30–90), SE (90–180), SW (180–250), and NW (250–30), respectively. In particular, we show brightness profiles for *Chandra* ACIS data in the top row and for the *XMM*-MOS data obtained from the reduction procedure proposed by Nevalainen et al. (2005) in the bottom row. The annuli width is $\sim 25''$, 50 pixels for *Chandra* ACIS data and 500 pixels for *XMM*-MOS data. Red, black, and green points represent total, net, and background brightness profiles, respectively.

Appendix C
Profiles

Here we present the complete set of gas and mass profiles obtained for the two sources discussed here. For NGC4649, in Figure 19 we show the surface brightness profiles, in Figures 20 and 21 we present the gas and mass profiles for fixed and variable abundances, and in Figure 22 we show the multicomponent fits to these mass profiles. For NGC 5846 these results are presented in Figures, 23, 24, 25, and 26, respectively.

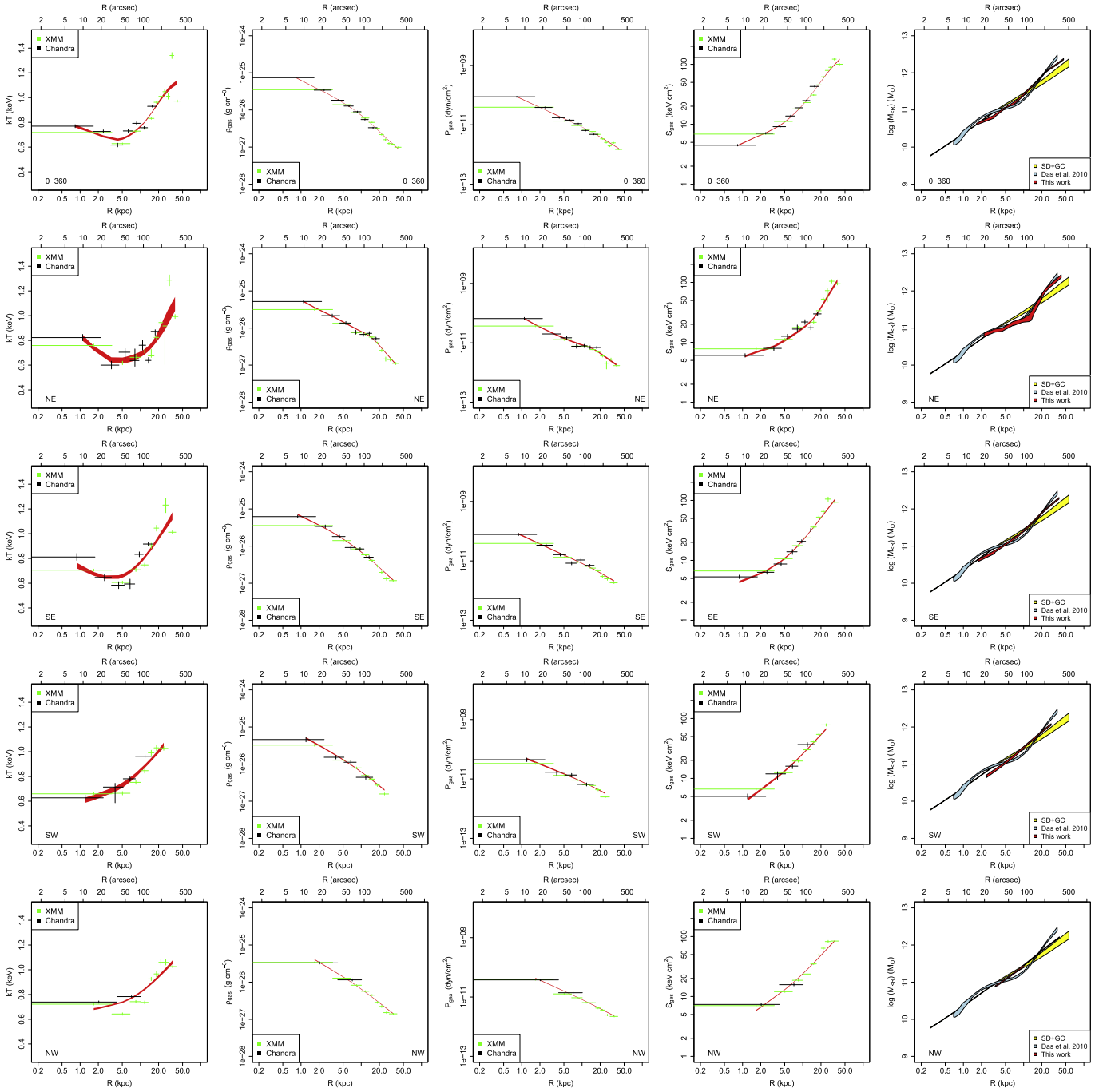

Figure 24. Gas profiles obtained in NGC 5846 with the reduction procedure proposed by Nevalainen et al. (2005). From top to bottom we show the profiles obtained in the full (0–360), NE (30–90), SE (90–180), SW (180–250), and NW (250–30) sectors, respectively. In each row we show from left to right the gas temperature, density, pressure, and entropy, respectively. Spectra extracted in the annuli are then simultaneously fitted (separately for *XMM* and *Chandra* data) with the fixed abundance model and deprojected using the PROJCT model. The annuli width is chosen to reach a signal-to-noise ratio of 30 for *XMM*-MOS data (represented in red) and of 50 for *Chandra* ACIS data (represented in black), with the exception of the full (0–360) sector, for which we chose a signal-to-noise ratio of 50 for *XMM* and 100 for *Chandra* data, and of the SW (250–30) sector, for which we use a signal-to-noise ratio of 50 for *XMM* and 50 for *Chandra* data. Best fits of a smooth cubic spline are presented in red, with smoothing parameter from top to bottom of 0.6, 0.6, 0.7, 0.7, and 0.7. In the rightmost panels in red we present the total mass profiles obtained by means of Equation (1) from the best fits to gas temperature and density profiles. In the same panels we show in yellow the optical mass profile obtained from SD and GC reported by Napolitano et al. (2014) and in light blue the X-ray mass profiles obtained by Das et al. (2010).

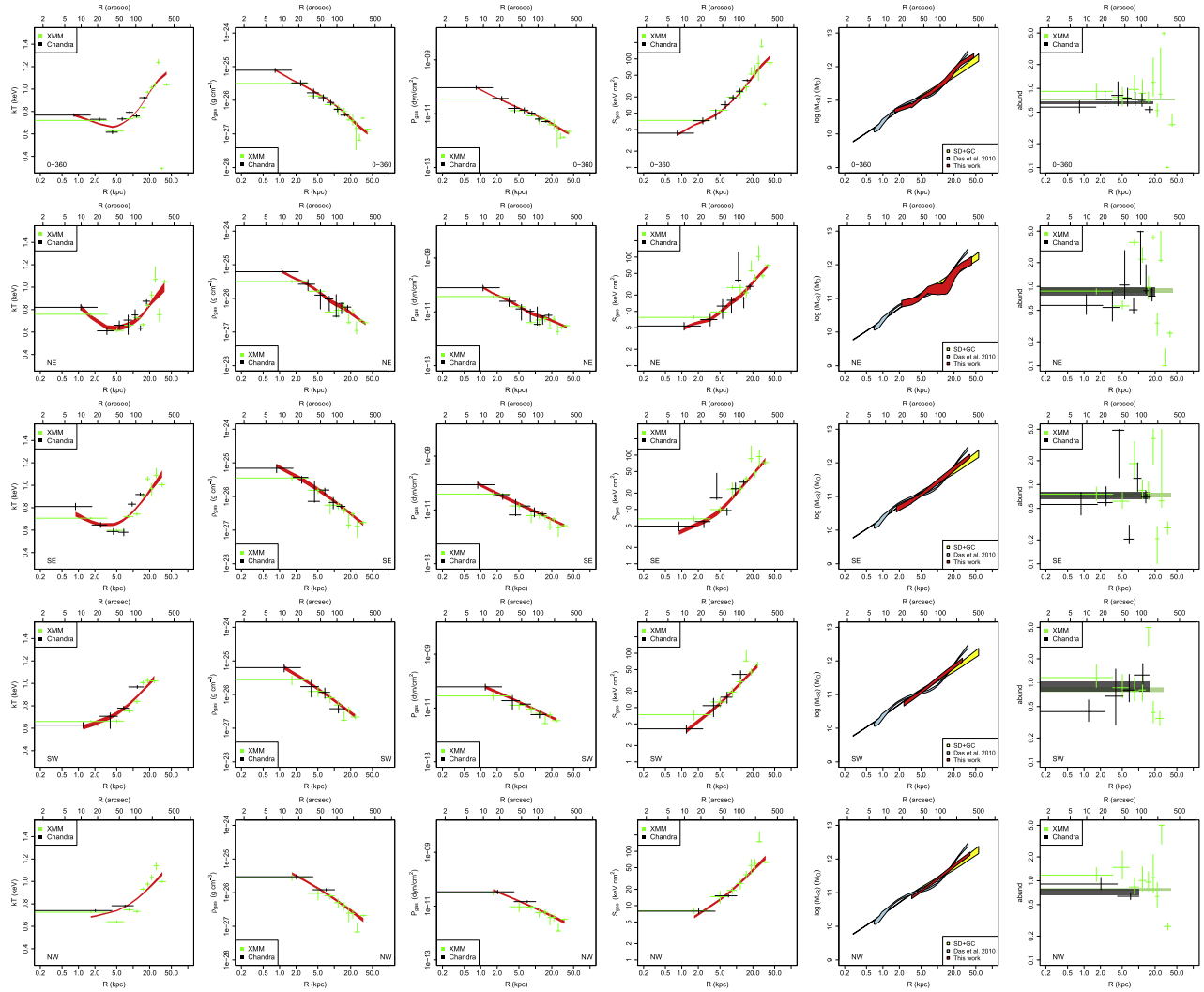

Figure 25. Same as Figure 24, but with the free abundance model. In addition, in the rightmost panel of each row we show the element abundance profiles for *XMM*-MOS data (in green) and for *Chandra* ACIS data (in black). In the same panels we overplot with green and black rectangles the values of the element abundances obtained with the fixed abundance model for *XMM* and *Chandra* data, respectively.

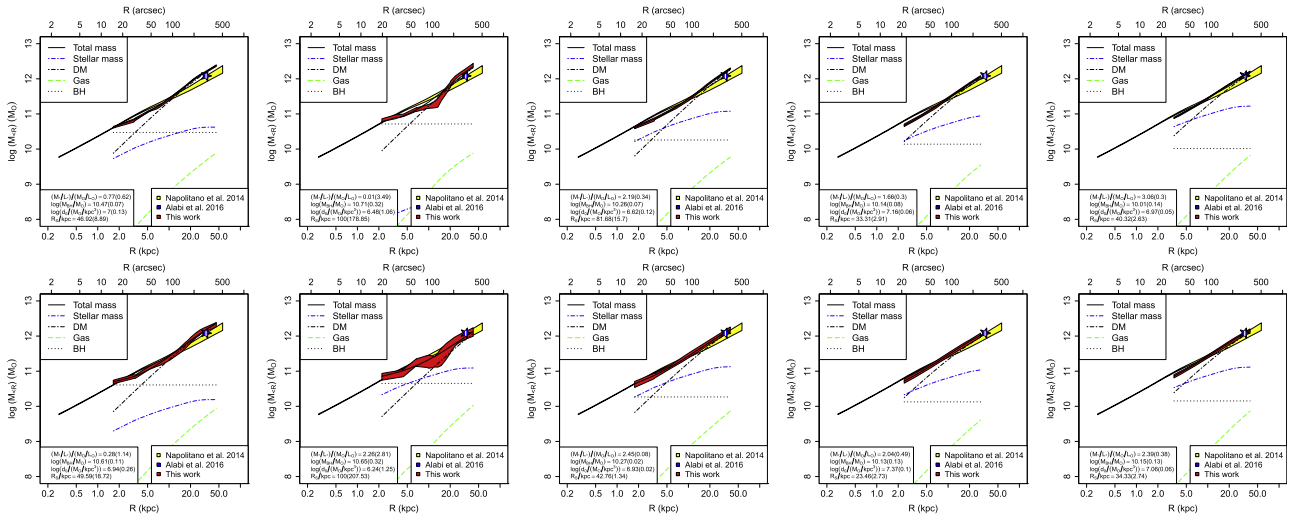

Figure 26. Fit to mass profiles of NGC 5846 shown in Figure 24 (top row) and in Figure 25 (bottom row), from left to right in the full (0–360), SE (120-180), and NW (250–30) sectors, respectively. The mass profile from the HE equation is presented in red, and the best-fit contributions of the various mass components (gas mass, stellar mass, black hole, and NFW DM profile) are presented with different colors as reported in the legend. The best-fit parameters are reported in the lower left box. In yellow we show the optical mass profile obtained from SD and GC reported by Napolitano et al. (2014), while the blue star represents the measurement by Alabi et al. (2016), with the corresponding uncertainty shown as a white vertical line inside the star itself.

References

Alabi, A. B., Forbes, D. A., Romanowsky, A. J., et al. 2016, MNRAS, 460, 3838
Arnaud, K. A. 1996, ASPC, 101, 17
Arnaud, M., Majerowicz, S., Lumb, D., et al. 2002, A&A, 390, 27
Arnaud, M., Neumann, D. M., Aghanim, N., et al. 2001, A&A, 365, L80
Ascasibar, Y., & Markevitch, M. 2006, ApJ, 650, 102
Auger, M. W., Treu, T., Gavazzi, R., et al. 2010, ApJL, 721, L163
Booth, C. M., & Schaye, J. 2010, MNRAS, 405, L1
Buote, D. A., & Humphrey, P. J. 2012, Astrophysics and Space Science Library, 378, 235
Canizares, C. R., Fabbiano, G., & Trinchieri, G. 1987, ApJ, 312, 503
Cappellari, M., McDermid, R. M., Alatalo, K., et al. 2013, MNRAS, 432, 1862
Cappellari, M., Romanowsky, A. J., Brodie, J. P., et al. 2015, ApJL, 804, L21
Carter, J. A., & Read, A. M. 2007, A&A, 464, 1155
Churazov, E., Forman, W., Vikhlinin, A., et al. 2008, MNRAS, 388, 1062
Churazov, E., Tremaine, S., Forman, W., et al. 2010, MNRAS, 404, 1165
Ciotti, L., D'Ercole, A., Pellegrini, S., & Renzini, A. 1991, ApJ, 376, 380
Ciotti, L., & Pellegrini, S. 2004, MNRAS, 350, 609
Coccato, L., Arnaboldi, M., & Gerhard, O. 2013, MNRAS, 436, 1322
Coccato, L., Gerhard, O., Arnaboldi, M., et al. 2008, AN, 329, 912
Condon, J. J., Cotton, W. D., & Broderick, J. J. 2002, AJ, 124, 675
D'Abrusco, R., Fabbiano, G., Mineo, S., et al. 2014, ApJ, 783, 18
Das, P., Gerhard, O., Churazov, E., & Zhuravleva, I. 2010, MNRAS, 409, 1362
Das, P., Gerhard, O., Coccato, L., et al. 2008, AN, 329, 940
Das, P., Gerhard, O., Mendez, R. H., Teodorescu, A. M., & de Lorenzi, F. 2011, MNRAS, 415, 1244
David, L. P., Forman, W., & Jones, C. 1990, ApJ, 359, 29
David, L. P., Forman, W., & Jones, C. 1991, ApJ, 369, 121
Deason, A. J., Belokurov, V., Evans, N. W., & McCarthy, I. G. 2012, ApJ, 748, 2
de Plaa, J., Zhuravleva, I., Werner, N., et al. 2012, A&A, 539, A34
Dunn, R. J. H., Allen, S. W., Taylor, G. B., et al. 2010, MNRAS, 404, 180
Emsellem, E., Cappellari, M., Krajnović, D., et al. 2011, MNRAS, 414, 888
Fabbiano, G., & Trinchieri, G. 1987, ApJ, 315, 46
Fabricant, D., Rybicki, G., & Gorenstein, P. 1984, ApJ, 286, 186
Finoguenov, A., Davis, D. S., Zimer, M., & Mulchaey, J. S. 2006, ApJ, 646, 143
Foster, C., Pastorello, N., Roediger, J., et al. 2016, MNRAS, 457, 147
Gastaldello, F., & Molendi, S. 2002, ApJ, 572, 160
Gehrels, N. 1986, ApJ, 303, 336
Graham, A. W. 2008, PASA, 25, 167
Grevesse, N., & Sauval, A. J. 1998, SSRv, 85, 161
Hickox, R. C., & Markevitch, M. 2006, ApJ, 645, 95
Humphrey, P. J., Buote, D. A., Brighenti, F., Gebhardt, K., & Mathews, W. G. 2008, ApJ, 683, 161
Humphrey, P. J., Buote, D. A., Brighenti, F., Gebhardt, K., & Mathews, W. G. 2013, MNRAS, 430, 1516
Irwin, J. A., Athey, A. E., & Bregman, J. N. 2003, ApJ, 587, 356
Johnson, R., Chakrabarty, D., O'Sullivan, E., & Raychaudhury, S. 2009, ApJ, 706, 980
Kim, D.-W., & Fabbiano, G. 2013, ApJ, 776, 116
Kim, D.-W., Fabbiano, G., & Trinchieri, G. 1992a, ApJS, 80, 645
Kim, D.-W., Fabbiano, G., & Trinchieri, G. 1992b, ApJ, 393, 134
Kronawitter, A., Saglia, R. P., Gerhard, O., & Bender, R. 2000, A&AS, 144, 53
Lal, D. V., Kraft, R. P., Randall, S. W., et al. 2013, ApJ, 764, 83
Loewenstein, M., & Davis, D. S. 2012, ApJ, 757, 121
Machacek, M. E., Jerius, D., Kraft, R., et al. 2011, ApJ, 743, 15
Mahdavi, A., Trentham, N., & Tully, R. B. 2005, AJ, 130, 1502
Markevitch, M., & Vikhlinin, A. 2007, PhR, 443, 1
Markevitch, M., Vikhlinin, A., & Mazzotta, P. 2001, ApJL, 562, L153
Memola, E., Salucci, P., & Babić, A. 2011, A&A, 534, A50
Mineo, S., Fabbiano, G., D'Abrusco, R., et al. 2014, ApJ, 780, 132
Napolitano, N. R., Pota, V., Romanowsky, A. J., et al. 2014, MNRAS, 439, 659
Navarro, J. F., Frenk, C. S., & White, S. D. M. 1997, ApJ, 490, 493
Nevalainen, J., Markevitch, M., & Lumb, D. 2005, ApJ, 629, 172
Ogorzalek, A., Zhuravleva, I., Allen, S. W., et al. 2017, arXiv:1702.04364
Paggi, A., Fabbiano, G., Kim, D.-W., et al. 2014, ApJ, 787, 134
Pellegrini, S., & Ciotti, L. 2006, MNRAS, 370, 1797
Pota, V., Brodie, J. P., Bridges, T., et al. 2015, MNRAS, 450, 1962
Roediger, E., Brüggen, M., Simionescu, A., et al. 2011, MNRAS, 413, 2057
Roediger, E., Kraft, R. P., Nulsen, P. E. J., et al. 2015a, ApJ, 806, 103
Roediger, E., Kraft, R. P., Nulsen, P. E. J., et al. 2015b, ApJ, 806, 104
Scott, N., Cappellari, M., Davies, R. L., et al. 2013, MNRAS, 432, 1894
Shen, J., & Gebhardt, K. 2010, ApJ, 711, 484
Shurkin, K., Dunn, R. J. H., Gentile, G., Taylor, G. B., & Allen, S. W. 2008, MNRAS, 383, 923
Snowden, S. L., & Kuntz, K. D. 2011, BAAS, 43, 344.17
Statler, T. S. 2012, Astrophysics and Space Science Library, 378, 207
Thomas, D., Maraston, C., Bender, R., & Mendes de Oliveira, C. 2005, ApJ, 621, 673
Tonry, J. L., Dressler, A., Blakeslee, J. P., et al. 2001, ApJ, 546, 681
Trinchieri, G., & Fabbiano, G. 1985, ApJ, 296, 447
Trinchieri, G., & Goudfrooij, P. 2002, A&A, 386, 472
Woods, R. A., Jones, C., Machacek, M. E., et al. 2017, arXiv:1703.05883
Zhu, L., Romanowsky, A. J., van de Ven, G., et al. 2016, MNRAS, 462, 4001
ZuHone, J. A., Markevitch, M., & Johnson, R. E. 2010, ApJ, 717, 908